

Variational system identification of the partial differential equations governing microstructure evolution in materials: Inference over sparse and spatially unrelated data

Z. Wang*, X. Huan[†] and K. Garikipati[‡]

February 2, 2021

Abstract

Pattern formation is a widely observed phenomenon in diverse fields including materials physics, developmental biology and ecology, among many others. The physics underlying the patterns is specific to the mechanisms, and is encoded by partial differential equations (PDEs). With the aim of discovering hidden physics, we have previously presented a variational approach to identifying such systems of PDEs in the face of noisy data at varying fidelities (*Computer Methods in Applied Mechanics and Engineering*, **353**:201-216, 2019). Here, we extend our variational system identification methods to address the challenges presented by image data on microstructures in materials physics. PDEs are formally posed as initial and boundary value problems over combinations of time intervals and spatial domains whose evolution is either fixed or can be tracked. However, the vast majority of microscopy techniques for evolving microstructure in a given material system deliver micrographs of pattern evolution over domains that bear no relation with each other at different time instants. The temporal resolution can rarely capture the fastest time scales that dominate the early dynamics, and noise abounds. Furthermore, data for evolution of the same phenomenon in a material system may well be obtained from different physical specimens. Against this backdrop of spatially unrelated, sparse and multi-source data, we exploit the variational framework to make judicious choices of weighting functions and identify PDE operators from the dynamics. A consistency condition arises for parsimonious inference of a minimal set of the spatial operators at steady state. It is complemented by a confirmation test that provides a sharp condition for acceptance of the inferred operators. The entire framework is demonstrated on synthetic data that reflect the characteristics of the experimental material microscopy images.

Keywords: Inverse problems, system identification, pattern formation, incomplete data

*Department of Mechanical Engineering, University of Michigan

[†]Department of Mechanical Engineering, Michigan Institute for Computational Discovery & Engineering, University of Michigan, University of Michigan

[‡]Departments of Mechanical Engineering, and Mathematics, Michigan Institute for Computational Discovery & Engineering, University of Michigan, corresponding author, krishna@umich.edu

1 Introduction

Pattern-formation is ubiquitous in many branches of the physical sciences. It occurs prominently in material microstructures driven by diffusion, reaction and phase transformations, and is revealed by a range of microscopy techniques that delineate the components or constituent phases. In developmental biology, examples include the organization of cells in the early embryo, markings on animal coats, insect wings, plant petals and leaves, as well as the segregation of cell types during the establishment of tissues. In ecology, patterns are formed on larger scales as types of vegetation spreads across forests. For context, we briefly discuss the role of pattern forming systems of equations in these phenomena. Pattern formation during phase transformations in materials physics can happen as the result of instability-induced bifurcations from a uniform composition [1, 2, 3], which was the original setting of the Cahn-Hilliard treatment [4]. Following Alan Turing’s seminal work on reaction-diffusion systems [5], a robust literature has developed on the application of nonlinear versions of this class of partial differential equations (PDEs) to model pattern formation in developmental biology [6, 7, 8, 9, 10, 11, 12, 13, 14]. The Cahn-Hilliard phase field equation has also been applied to model other biological processes with evolving fronts, such as tumor growth and angiogenesis [15, 16, 17, 18, 19, 20, 21, 22]. Reaction-diffusion equations also appear in ecology, where they are more commonly referred to as activator-inhibitor systems, and are found to underlie large scale patterning [23, 24]. All of these pattern forming systems fall into the class of nonlinear, parabolic PDEs, and have spawned a vast literature in mathematical physics. They can be written as systems of first-order dynamics driven by a number of time-independent terms of algebraic and differential form. The spatio-temporal, differentio-algebraic operators act on either a composition (normalized concentration) or an order parameter. It also is common for the algebraic and differential terms to be coupled across multiple species.

Patterns in physical systems are of interest because, up to a point, human experts in each of the above fields (materials microscopists, developmental biologists and ecologists) are able to identify phenomena solely on the basis of patterns. This success of intuition fed by experience does, however, break down when, for instance, the materials scientist is confronted by the dynamic processes in an unstudied alloy, or the developmental biologist considers a previously neglected aspect of morphogenesis. In such settings the challenge is to discover the operative physics from among a range of mechanisms. As with all of quantitative physics, the only rigorous route to such discovery is the mathematical one. For systems that vary over space and time, this description is in the form of PDEs. Identification of participating PDE operators from spatio-temporal observations can thus uncover the underlying physical mechanisms, and lead to improved understanding, prediction and manipulation of these systems.

Distinct from classical adjoint-based approaches to inverse problems, the system identification problem on PDEs is to balance accuracy and complexity in finding the best model among many possible candidates that could explain the spatio-temporal data on the dynamical system. The

proposed models can be parameterized by the coefficients of candidate operators, which serve as a basis. The task of solving this inverse problem can then be posed as finding the best coefficient values that allow a good agreement between model predictions and data. Sparsity of these coefficients is further motivated by the principle that parsimony of physical mechanisms is favored for applicability to wider regimes of initial and boundary value problems. The comparison procedure between models and data may be set up via the following two broad approaches. (a) When only sparse and noisy data are available, which might also be of indirect quantities that do not explicitly enter the PDEs, quantifying uncertainty in the identification becomes important and a Bayesian statistical approach is very useful. (b) When relatively larger volumes of observed data are accessible for quantities that directly participate in the PDEs, regression-based methods seeking to minimize an appropriate loss function can be highly efficient.

The first (Bayesian) approach has been successfully used for inferring a fixed number of coefficients in specified PDE models, leveraging efficient sampling algorithms such as Markov Chain Monte Carlo [25]. However, they generally require many forward solutions of the PDE models, which is computationally expensive and may quickly become impractical with growth in the number of PDE terms (i.e., dimension of the identification problem). As a result, the use of Bayesian approaches for identifying the best model from a large candidate set remains challenging. If made practical, they can be advantageous in providing uncertainty information, and offering significant flexibility in accommodating the data, which could be sparse and noisy, only available over some subset of the domain, collected at a few time steps, and composed of multiple statistical measures, functionals of the solution, or other indirect Quantities of Interests (QoIs). In the second (regression) approach, the PDEs themselves have to be represented by the data, which can be achieved by constructing the operators either in strong form such as finite difference, as in the Sparse Identification of Nonlinear Dynamics (SINDy) approach [26], or in weak form built upon basis functions, as in the Variational System Identification (VSI) approach [27]. Both representations pose stringent requirements on the data for accurately constructing the operators. The first of these is the need for time series data that can be related to chosen spatial points either directly or by interpolation. This is essential for consistency with a PDE that is written in terms of spatio-temporal operators at defined points in space and instants in time. The second requirement is for data with sufficient spatial resolution to construct spatial differential operators of possibly high order. However, these regression approaches enjoy the advantage over Bayesian methods that repeated forward PDE solutions are not necessary. PDE operators have thus been successfully identified from a comprehensive library of candidates [26, 27, 28, 29]. In a different approach to solving inverse problems [30], the strong form of a specified PDE is directly embedded in the loss function while training deep neural network representations of the solution variable. However, this approach depends on data at high spatial and temporal resolution for successful training of the deep neural network representations of the solution variable. A perspective and comparison between these two approaches

can be found in Ref. [31]. Lastly, there has been growing interest in combining graph theory with data-driven physics discovery. These approaches include genetic programming algorithm for discovering governing equations without pre-specification of the operators [32], and geometric learning for reconstructing the normal forms of equations using data collected from systems with unknown initial conditions and parameter values [33].

A significant discordance can exist in the form of material microstructure datasets when juxtaposed against the underlying premise of all the above approaches. These experimental datasets, while corresponding to different times are also commonly collected over different spatial subdomains of a physical specimen at each instant. This includes scenarios where the spatial subdomains have no overlap and are unrelated to each other. Furthermore, while subject to the same processing conditions, they may well come from different physical specimens. This is because the experimental techniques for extracting data at a given time after specimen preparation (which can include mechanical, chemical and thermal steps) involve destructive processes including cutting and grinding of the specimen. After this procedure, the entire specimen is removed from further experimentation, and a new specimen needs to be created if data is to be collected at a different time. Both of these conditions essentially negate the foundational notion of a PDE describing the temporal evolution of quantities at chosen spatial points for a single instantiation of that initial and boundary value problem (IBVP). The spatial subdomains on which microscopy is conducted may represent only small portions of entire specimens. Boundary data, if present, are also prey to the above loss of spatial localization over time. Finally, the effort of processing (specimen preparation, mechanical, chemical and heat treatment) to attain the desired kinetic rates and thermodynamic driving forces, and subsequently to obtain microscopy images, leads to sparsity of data in time; even tens of instants are uncommon.

In this communication, we extend our VSI methods [27] to sparse and spatially unrelated data, motivated by the above challenges of experimental microscopy in materials physics. The goal remains to discover the physical mechanisms underlying patterns of diffusion, reaction and phase transformation in materials physics. We present novel advances that exploit the variational framework and a notion of similarity between *snapshots* of data, which we make precise, to circumvent the loss of spatial relatedness so that temporally sparse data prove sufficient for inferring the kinetics. These methods are described in Section 2 and demonstrated on synthetic data in Section 2.6. Furthermore, imposition of consistency on the steady state versions of candidate PDEs opens the door to parsimonious choice of a minimal set of spatial operators. To complement this condition, we also present a confirmation test that is a sharp condition for acceptance of the inferred operators. The confirmation test is described in Section 3 and demonstrated on synthetic data in Section 3.2. Discussions and concluding remarks are presented in Section 4.

2 Variational identification of PDE systems from sparse and spatially unrelated data

2.1 The Galerkin weak form for system identification

We first provide a brief discussion on the weak form of PDEs as used in this work. We start with the general strong form for first-order dynamics written as

$$\frac{\partial C}{\partial t} - \boldsymbol{\chi} \cdot \boldsymbol{\theta} = 0, \quad (1)$$

where $\boldsymbol{\chi}$ is a vector containing all possible linearly independent terms expressed as algebraic and differential operators on the scalar solution C :

$$\boldsymbol{\chi} = [1, C, C^2, \dots, \nabla^2 C, \dots], \quad (2)$$

and $\boldsymbol{\theta}$ is the vector of scalar coefficients of these operators. For example, using this nomenclature, the one-field diffusion reaction equation

$$\frac{\partial C}{\partial t} - D \nabla^2 C - f = 0 \quad (3)$$

with constant diffusivity D and reaction rate f has

$$\boldsymbol{\chi} = [1, C, C^2, \nabla^2 C] \quad \text{and} \quad \boldsymbol{\theta} = [f, 0, 0, D]. \quad (4)$$

Note that the time derivative $\partial C / \partial t$ is treated separately from the other terms in order to highlight the first-order dynamics of the problems that we target in this work. Given some observational data for the dynamical system, our system identification problem entails finding the correct governing equation via the coefficient vector, $\boldsymbol{\theta}$, which specifies the active operators from among a dictionary of candidates, $\boldsymbol{\chi}$.

As argued by Wang et al. [27], the weak form offers particular advantages for the system identification problem. It allows the use of basis functions that can be drawn from function classes that have higher-order regularity. Furthermore, the weak form transfers spatial derivative operators from the trial solution, represented by the data on C , to the weighting function. These two features significantly mollify the noise, stiffness and general loss of robustness associated with constructing spatial derivatives from data. They are especially relevant for the consideration of high-order gradient operators, which are often found in many types of pattern-forming phenomena in physics. Another advantage of writing the PDEs in weak form is that boundary conditions can be constructed as operators, thus making their identification a natural outcome. This weak form approach then leads to what we refer to as Variational System Identification [27], abbreviated here to VSI. We note that, very recently, there has been growing interest in exploiting the weak form for system identification in numerical [34] as well as analytical settings [35, 36].

For infinite-dimensional problems with Dirichlet boundary conditions on Γ^c , the weak form is stated as: $\forall w \in \mathcal{V}$ where $\mathcal{V} = \{w \mid w = 0 \text{ on } \Gamma^c\}$, find $C \in \mathcal{S}$ where $\mathcal{S} = \{C \mid C = \bar{C} \text{ on } \Gamma^c\}$ such that

$$\int_{\Omega} w \left(\frac{\partial C}{\partial t} - \boldsymbol{\chi} \cdot \boldsymbol{\theta} \right) dv = 0. \quad (5)$$

Integration by parts and the application of boundary conditions, which are determined by the operators in $\boldsymbol{\chi}$, leads to the final weak form. In the interest of brevity we have not written out the weak form for each instance of $\boldsymbol{\chi}$. For finite-dimensional fields, C^h and w^h , respectively, replace C and w in the statement of Equation (5): $C^h \in \mathcal{S}^h \subset \mathcal{S}$ where $\mathcal{S}^h = \{C^h \in \mathcal{H}^2(\Omega) \mid C^h = \bar{C} \text{ on } \Gamma^u\}$, and $w^h \in \mathcal{V}^h \subset \mathcal{V}$ where $\mathcal{V}^h = \{w^h \in \mathcal{H}^2(\Omega) \mid w^h = 0 \text{ on } \Gamma^u\}$. The choice of $\mathcal{H}^2(\Omega)$ as the Sobolev space is motivated by the differential operators, which reach the highest order of two in the weak forms we consider (and order four in strong form). The variations w^h and trial solutions C^h are defined component-wise using a finite number of basis functions:

$$w^h = \sum_{a=1}^{n_b} d^a \phi^a \quad (6)$$

$$C^h = \sum_{a=1}^{n_b} c^a \phi^a, \quad (7)$$

where n_b is the dimensionality of the function spaces \mathcal{S}^h and \mathcal{V}^h , and ϕ^a represents the basis functions. Equation (7) represents interpolation of discrete data to obtain fields with regularity specified by \mathcal{H}^2 .

If, at each time instant of interest, t , the data available are in the form $C(\boldsymbol{x}_I, t)$ such that $\boldsymbol{x}_I \in \Omega$ for $I = 1, \dots, n_{\text{sp}}$, with n_{sp} being the number of spatial points—that is, if data is available corresponding to discretization points for the entire spatial domain—then VSI as presented in its original framework [27] presents itself as a powerful approach. However, the experimental characterization of microstructure evolution is typically carried out on physical samples that are cut out of larger wafers at chosen times, further processed for microscopy and then discarded. For this reason, the data acquired at each time are only available over subdomains of the full field that do not correspond to the same spatial locations—i.e., they are spatially unrelated (Figure 1), as explained in the Introduction. For brevity we use the term *snapshot* to refer to the data field over a chosen subdomain and at a given time. For experimental convenience, these snapshots are typically rectangular—a fact that we leverage for our methods. Furthermore, each such snapshot is usually produced from a different physical specimen due to the destructive and intrusive nature of data acquisition in the experiments. We next present a two-stage approach that accommodates these scenarios by exploiting the variational setting.

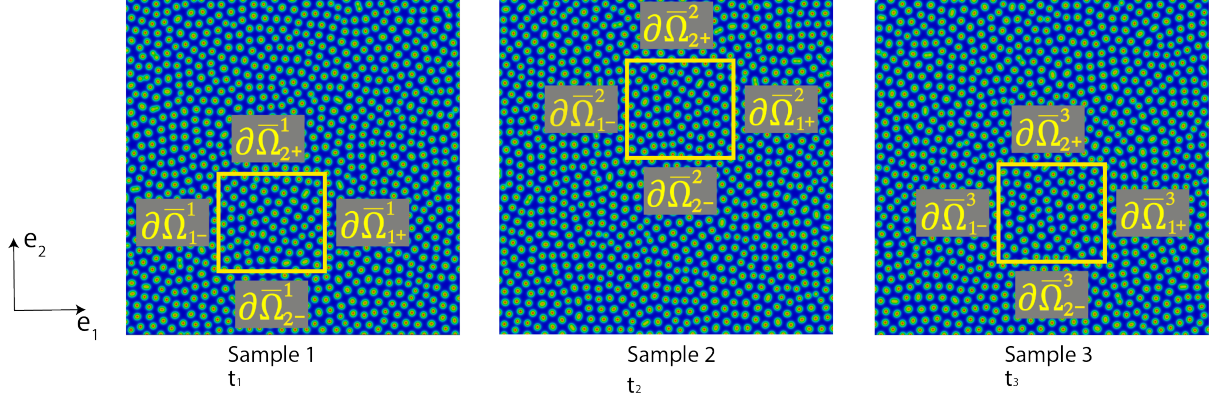


Figure 1: The sample data shown within the snapshots (yellow square) corresponding to each time instant are only available over subdomains of the full field. They are also spatially unrelated over time.

2.2 Similarity of snapshots

The snapshots are chosen to be sufficiently distant from boundaries of the wafer so that they are representative of any other region, also similarly removed from the boundaries. If such rectangular snapshots (typically used for experimental characterization), say $\bar{\Omega}^1, \bar{\Omega}^2, \bar{\Omega}^3, \dots$ are identical in geometry and subject to periodic boundary conditions on $\partial\bar{\Omega}_i^I$, where $I = 1, 2, 3, \dots$, and $i = 1, 2$ denotes coordinate planes relative to which the boundaries $\partial\bar{\Omega}_i^I$ are perpendicular (see Figure 1), it follows that the field C is identical within $\bar{\Omega}^1, \bar{\Omega}^2, \bar{\Omega}^3, \dots$. However, this condition requiring identical physical samples is too strong to impose on the experimental techniques. Instead, two weaker conditions are assumed to hold. The first states that for rectangular and identical snapshots, $\bar{\Omega}^I, \bar{\Omega}^J$, the mass influxes, j_n , integrated over the corresponding boundary subsets, $\partial\bar{\Omega}_{i+}^I, \partial\bar{\Omega}_{i+}^J$ or $\partial\bar{\Omega}_{i-}^I, \partial\bar{\Omega}_{i-}^J$, $i = 1, 2$ respectively, are equal (see Figure 1):

$$\int_{\partial\bar{\Omega}_{i\pm}^I} j_n dS = \int_{\partial\bar{\Omega}_{i\pm}^J} j_n dS, \quad i = 1, 2. \quad (8)$$

By choosing $\bar{\Omega}^I, \bar{\Omega}^J$ to be adjacent with a common boundary, say $\partial\bar{\Omega}_{i+}^I = \partial\bar{\Omega}_{i-}^J$, noting that the influx $j_n = -\mathbf{j} \cdot \mathbf{n}$ for flux \mathbf{j} and unit outward normal to a boundary being \mathbf{n} we have :

$$-\int_{\partial\bar{\Omega}_{i+}^I} \mathbf{j} \cdot \mathbf{n} dS = -\int_{\partial\bar{\Omega}_{i+}^J} \mathbf{j} \cdot \mathbf{n} dS = \int_{\partial\bar{\Omega}_{i-}^J} \mathbf{j} \cdot \mathbf{n} dS, \quad i = 1, 2. \quad (9)$$

Where, by virtue of being the unit outward normal, \mathbf{n} over $\partial\bar{\Omega}_{i+}^I$ is opposite to \mathbf{n} over $\partial\bar{\Omega}_{i-}^J$. From the last two members of the above equation, we have:

$$\int_{\partial\bar{\Omega}_i^J} \mathbf{j} \cdot \mathbf{n} dS = \int_{\partial\bar{\Omega}_{i+}^J} \mathbf{j} \cdot \mathbf{n} dS + \int_{\partial\bar{\Omega}_{i-}^J} \mathbf{j} \cdot \mathbf{n} dS = 0, \quad i = 1, 2. \quad (10)$$

This means that the total mass fluxes integrated over opposite boundaries are equal and opposite, thus ensuring that the total mass flowing in over one boundary exits over the opposite one. This implies the vanishing of mass flux upon integration over the boundary

$$\int_{\partial\bar{\Omega}^I} \mathbf{j} \cdot \mathbf{n} dS = 0 \quad (11)$$

for an arbitrary snapshot $\bar{\Omega}^I$.

As the second condition we assume that volume-averaged k^{th} powers of the composition field are equal between the rectangular snapshots:

$$\frac{1}{\bar{V}^1} \int_{\bar{\Omega}^1} C^k dV = \frac{1}{\bar{V}^2} \int_{\bar{\Omega}^2} C^k dV = \frac{1}{\bar{V}^3} \int_{\bar{\Omega}^3} C^k dV = \dots \quad (12)$$

where $\bar{V}^I = \text{vol}(\bar{\Omega}^I)$. In practice, Equations (11) and (12) are expected to hold approximately, so that

$$\left| \int_{\bar{\Omega}^I} \mathbf{j} \cdot \mathbf{n} dS \right| \leq \varepsilon_{\text{b}}, \quad i = 1, 2 \quad (13)$$

and

$$\left| \frac{1}{\bar{V}^I} \int_{\bar{\Omega}^I} C^k dV - \frac{1}{\bar{V}^J} \int_{\bar{\Omega}^J} C^k dV \right| \leq \varepsilon_{\text{r}} \quad (14)$$

for $0 < \varepsilon_{\text{b}}, \varepsilon_{\text{r}}$ being bounded. Equations (13) and (14) represent the notion of similarity that is assumed between snapshots used for material characterization. Since the methods developed in this communication are concerned with such experiments, we use this notion of similarity in developing variational system identification techniques in the following section. Additionally, Section 2.6.2 demonstrates the approximate satisfaction of Equations (13) and (14) for the class of first-order PDEs that govern the evolution of microstructure in materials.

2.3 Two stage variational system identification for dynamics

First, we rewrite Equation (5) as an integral over $\Omega_n \subseteq \Omega$; a subset representing the snapshot over which data was acquired at time t_n . Additionally, we split operators $\boldsymbol{\chi}$ and coefficients $\boldsymbol{\theta}$ into two parts such that $\boldsymbol{\chi} \cdot \boldsymbol{\theta} = \boldsymbol{\chi}_1 \cdot \boldsymbol{\theta}_1 + \boldsymbol{\chi}_2 \cdot \boldsymbol{\theta}_2$. The entire equation is furthermore normalized by $V_n = \text{vol}(\Omega_n)$:

$$\frac{1}{V_n} \int_{\Omega_n} w \left(\frac{\partial C}{\partial t} - (\boldsymbol{\chi}_1 \cdot \boldsymbol{\theta}_1 + \boldsymbol{\chi}_2 \cdot \boldsymbol{\theta}_2) \right) dv = 0. \quad (15)$$

Here, the components of χ_1 contain all the algebraic operators and those of χ_2 contain all the differential operators:

$$\chi_1 = [1, C, C^2, \dots], \quad \chi_2 = [\nabla^2 C, \nabla \cdot C \nabla C, \nabla^4 C, \dots], \quad (16)$$

with θ_1 and θ_2 being the corresponding coefficient vectors. We then use a backward difference approximation of the dynamics, write $\chi_2 \cdot \theta_2$ in divergence form as $\chi_2 \cdot \theta_2 = \nabla \cdot (\hat{\chi}_2 \cdot \hat{\theta}_2)$ and apply integration by parts to arrive at:

$$\frac{1}{V_n} \int_{\Omega_n} w \frac{C_n - C_{n-1}}{\Delta t} dv = \frac{1}{V_n} \left(\int_{\Omega_n} w \chi_{1n} dv \cdot \theta_1 - \int_{\Omega_n} \nabla w \cdot \hat{\chi}_{2n} dv \cdot \hat{\theta}_2 + \int_{\partial\Omega_n} w \hat{\chi}_{2n} \cdot \mathbf{n} ds \cdot \hat{\theta}_2 \right), \quad (17)$$

where $(\bullet)_n$ denotes the time discrete approximation of a field at time t_n . While other time-marching schemes are certainly also possible, we use backward differencing here for its simplicity, stability, and as a representative choice for illustration purposes when the focus of our problem is not on time-marching specifically. While, with noise-free data, the time discrete approximation grows more accurate for smaller time steps, noise could be amplified by the time discretization and overwhelm the true value [27]. Larger time steps can prevent this dominance of the noise.

We define Stage 1 by choosing $w = 1$, yielding:

$$\frac{1}{V_n} \int_{\Omega_n} C_n dv = \frac{1}{V_n} \Delta t \int_{\Omega_n} \chi_{1n} dv \cdot \theta_1 + \frac{1}{V_n} \int_{\Omega_n} C_{n-1} dv + \frac{1}{V_n} \Delta t \int_{\partial\Omega_n} \hat{\chi}_{2n} \cdot \mathbf{n} ds \cdot \hat{\theta}_2 \quad (18)$$

The left hand-side is the mean composition field. The $\hat{\chi}_2$ operators vanish in volume integrands since, for a constant weighting function, $\nabla w = 0$. From Equation (13) the boundary term on the right satisfies

$$\frac{1}{V_n} \Delta t \int_{\partial\Omega_n} \hat{\chi}_{2n} \cdot \mathbf{n} ds \cdot \hat{\theta}_2 \leq \frac{\varepsilon_b \Delta t}{V_n}, \quad (19)$$

and for small enough ε_b can be neglected relative to the other terms of order $\Delta t/V_n$. See Section 2.6.2 for numerical evidence of this result for similarity of snapshots. As a consequence, only algebraic (non-differential) operators remain:

$$\frac{1}{V_n} \int_{\Omega_n} C_n dv = \frac{1}{V_n} \Delta t \int_{\Omega_n} \chi_{1n} dv \cdot \theta_1 + \frac{1}{V_n} \int_{\Omega_n} C_{n-1} dv. \quad (20)$$

For Stage 2, we choose $w = C_n$ over Ω_n , to give:

$$\frac{1}{V_n} \int_{\Omega_n} C_n \frac{\partial C_n}{\partial t} dv = \frac{1}{V_n} \int_{\Omega_n} C_n \chi \cdot \theta dv \quad (21)$$

$$\Rightarrow \frac{1}{V_n} \int_{\Omega_n} \frac{1}{2} \frac{\partial C_n^2}{\partial t} dv = \frac{1}{V_n} \int_{\Omega_n} C_n \chi \cdot \theta dv \quad (22)$$

$$= \frac{1}{V_n} \int_{\Omega_n} C_n \chi_1 \cdot \theta_1 dv + \frac{1}{V_n} \int_{\Omega_n} C_n \chi_2 \cdot \theta_2 dv. \quad (23)$$

Again writing a backward difference approximation of the dynamics, using the divergence form as above and integrating by parts, we have:

$$\begin{aligned} \frac{1}{V_n} \int_{\Omega_n} C_n^2 dv &= \frac{1}{V_n} 2\Delta t \left(\int_{\Omega_n} C_n \chi_{1n} dv \cdot \boldsymbol{\theta}_1 - \int_{\Omega_n} \nabla C_n \cdot \widehat{\chi}_{2n} dv \cdot \widehat{\boldsymbol{\theta}}_2 \right) \\ &\quad + \frac{1}{V_n} 2\Delta t \int_{\partial\Omega_n} C_n \widehat{\chi}_{2n} \cdot \mathbf{n} ds \cdot \widehat{\boldsymbol{\theta}}_2 + \frac{1}{V_n} \int_{\Omega_n} C_{n-1}^2 dv. \end{aligned} \quad (24)$$

The left hand-side of Equation (24) is the second power of the concentration field. Note that the boundary term is different than in Equation (18), and cannot be assumed to vanish. Before moving on with the formulation we emphasize that $\Omega_n \subseteq \Omega$ in Equations (20) and (24) can be the entire physical specimen, Ω , or any subdomain.

Relation (14) guarantees that the volume-normalized first and second powers of C_n over a chosen subdomain can be approximated by the corresponding volume-normalized powers evaluated over different subdomains. We can thus write

$$\frac{1}{V_{i_n}} \int_{\Omega_{i_n}} C_n^k dv \approx \frac{1}{V_{j_n}} \int_{\Omega_{j_n}} C_n^k dv, \quad \text{where } \Omega_{i_n}, \Omega_{j_n} \subseteq \Omega, \quad i, j = 1, 2, \dots \quad (25)$$

Equation (25) allows us to use data collected over different subdomains, Ω_{i_n} , $i = 1, 2, \dots$ at time t_n . This further allows us to estimate the volume-normalized powers by replacing the integrals of C_{n-1} and C_{n-1}^2 over Ω_n in Equations (20) and (24), respectively, by integrals of the same integrands, but over Ω_{n-1} :

$$\frac{1}{V_n} \int_{\Omega_n} C_n dv \approx \frac{1}{V_n} \Delta t \int_{\Omega_n} \chi_1 dv \cdot \boldsymbol{\theta}_1 + \frac{1}{V_{n-1}} \int_{\Omega_{n-1}} C_{n-1} dv \quad (26)$$

$$\begin{aligned} \frac{1}{V_n} \int_{\Omega_n} C_n^2 dv &\approx \frac{1}{V_n} 2\Delta t \left(\int_{\Omega_n} C_n \chi_1 dv \cdot \boldsymbol{\theta}_1 - \int_{\Omega_n} \nabla C_n \cdot \widehat{\chi}_2 dv \cdot \widehat{\boldsymbol{\theta}}_2 \right) + \frac{1}{V_{n-1}} \int_{\Omega_{n-1}} C_{n-1}^2 dv \\ &\quad + \frac{1}{V_n} 2\Delta t \int_{\partial\Omega_n} C_n \widehat{\chi}_{2n} \cdot \mathbf{n} ds \cdot \widehat{\boldsymbol{\theta}}_2 \end{aligned} \quad (27)$$

Thus, the data C_k corresponding to a specific time instant, t_k , need only be considered over the snapshot, Ω_k , observed at that time in an experiment.

Relation (14) also guarantees that the volume-normalized first and second powers of C_n over sub-domain Ω_n at time t_n can be approximated by the corresponding volume-normalized powers evaluated using data, \tilde{C}_n , collected from sub-domains $\tilde{\Omega}$ on *different physical specimens* at time t_n . Here, the tilde denotes data from a different specimen. This reflects experimental practice in which data from different specimens are measured under the same conditions and physical time of the experiment, and similarity of snapshots is assumed. The mathematical and numerical equivalence to this procedure is modeled by employing the same initial condition with different

spatially randomized perturbations. This is explained in detail in Section 2.6.1. We can then write

$$\frac{1}{V_n} \int_{\Omega_n} C_n^k dv \approx \frac{1}{\tilde{V}_n} \int_{\tilde{\Omega}_n} \tilde{C}_n^k dv. \quad (28)$$

Relation (14) is a statement on the similarity of fields over different subdomains and physical specimens at the same time. The data collected from pattern forming phenomena better satisfies this approximation of similarity for larger subdomains because localized features are averaged out. The extent to which the similarity implied in relations (13) and (14) is realized in the data is discussed in Section 2.6.2. Replacing the approximations by equalities in our VSI algorithm, Equations (26) and (27) can be rewritten as:

Stage 1:

$$\frac{1}{\Delta t} \left(\frac{1}{V_n} \int_{\Omega_n} C_n dv - \frac{1}{V_{n-1}} \int_{\Omega_{n-1}} C_{n-1} dv \right) = \frac{1}{V_n} \int_{\Omega_n} \chi_1 dv \cdot \theta_1 \quad (29)$$

Stage 2:

$$\begin{aligned} \frac{1}{2\Delta t} \left(\frac{1}{V_n} \int_{\Omega_n} C_n^2 dv - \frac{1}{V_{n-1}} \int_{\Omega_{n-1}} C_{n-1}^2 dv \right) - \frac{1}{V_n} \int_{\Omega_n} C_n \chi_1 dv \cdot \theta_1 &= -\frac{1}{V_n} \int_{\Omega_n} \nabla C_n \cdot \hat{\chi}_2 dv \cdot \hat{\theta}_2 \\ + \frac{1}{V_n} \int_{\partial\Omega_n} C_n \hat{\chi}_{2n} \cdot \mathbf{n} ds \cdot \hat{\theta}_2 & \end{aligned} \quad (30)$$

where, following Equation (28), the fields C_n, C_{n-1} and sub-domains Ω_n, Ω_{n-1} could come from any specimen, and we have dispensed with the tildes. Given data on C at suitable times, we define the left hand-sides of Equations (29) and (30) to be the labels. In Section 2.5 we show how they lead to target vectors in VSI, and the right hand-sides lead to matrices of candidate basis operators.

We recall that, in the weak form, the choice of the weighting function $w^h \in \mathcal{V}^h$ is arbitrary. However, the judicious choice of w^h is critical for the success of VSI. A spatially constant w^h eliminates volume integrals of differential operators in the weak form leaving only algebraic (non-differential) operators as volume terms in Stage 1. The choice of $w^h = C^h$ in Stage 2 turns differential operators, such as the Laplace and biharmonic operators into quadratic forms in the weak form (see Section 2.4 below). This is suitable for pattern forming dynamics, because it ensures that the integrand of, e.g. $\int_{\Omega} \nabla C \cdot \nabla C dv$ is non-negative, and that the corresponding weak operators are identifiable. However certain choices of w^h could render some operators unidentifiable. For example, choosing $w^h = x_1$ (spatial coordinate), the integral $\int_{\Omega} \nabla x_1 \cdot \nabla C dv$ proves insignificant when evaluated over a (quasi-)periodic pattern. Contributions to this term are nearly cancelled out by the x_1 -symmetry of the (quasi-)periodicity that is seen, for instance, in Figure 1.

2.4 Candidate basis operators

Suppose we have data on certain degrees of freedom (DOFs) of a discretization, C^h , for a series of time steps. These DOFs are the nodal values in finite element methods, and the control variables if iso-geometric analytic methods are used. Using these DOFs, a Galerkin representation of the field could be constructed over the domain. Below we explain the procedure of generating candidate basis operators in weak form with three examples.

2.4.1 Weak forms of polynomial approximations of algebraic operators at time t_n with $w^h = 1$

$$\chi_{1_n}^{C^k, 1} = \frac{1}{V_n} \int_{\Omega_n} (C_n^h)^k dv \quad (31)$$

The above equation represents all algebraic operators without loss of generality, since in principle they can all be expanded via polynomial expansions (e.g., Taylor series). If specific forms are desired, for instance exponential terms that are common in reaction terms, they would be used directly. While $w^h = C^h$ (and higher powers) does not eliminate algebraic operators in Stage 2, $w^h = 1$ does eliminate differential operators from the volume integrals allowing robust identification of the algebraic operators in Stage 1.

2.4.2 Weak form of the Laplacian operator at time t_n with $w^h = C^h$

Multiplying by the weighting function and integrating by parts, we have

$$\int_{\Omega_n} C_n^h \nabla^2 C_n^h dv = - \int_{\Omega_n} \nabla C_n^h \cdot \nabla C_n^h dv + \frac{1}{2} \int_{\partial\Omega_n} \nabla (C_n^h)^2 \cdot \mathbf{n} ds. \quad (32)$$

We define

$$\chi_{2_n}^{\nabla^2 C, C} = - \int_{\Omega_n} \nabla C_n^h \cdot \nabla C_n^h dv + \frac{1}{2} \int_{\partial\Omega_n} \nabla (C_n^h)^2 \cdot \mathbf{n} ds \quad (33)$$

as the Laplacian in weak form with $w^h = C^h$.

2.4.3 Weak form of the biharmonic operator $\nabla^4 C_n$ at time t_n with $w^h = C^h$

Multiplying by the weighting function and integrating by parts twice, we obtain

$$\int_{\Omega_n} w^h \nabla^4 C_n^h dv = \int_{\Omega_n} \nabla^2 C_n^h \nabla^2 C_n^h dv - \int_{\partial\Omega_n} \nabla C_n^h \cdot \mathbf{n} \nabla^2 C_n^h ds + \int_{\partial\Omega_n} C_n^h \nabla (\nabla^2 C_n^h) \cdot \mathbf{n} ds. \quad (34)$$

We then define

$$\chi_{2_n}^{\nabla^4 C, C} = \int_{\Omega_n} \nabla^2 C_n^h \nabla^2 C_n^h dv - \int_{\partial\Omega_n} \nabla C_n^h \cdot \mathbf{n} \nabla^2 C_n^h ds + \int_{\partial\Omega_n} C_n^h \nabla (\nabla^2 C_n^h) \cdot \mathbf{n} ds \quad (35)$$

as the biharmonic operator in weak form with $w^h = C^h$.

The second-order gradients in Equation (35) require the solutions and basis functions to lie in $\mathcal{H}^2(\Omega)$, while the Lagrange polynomial basis functions traditionally used in finite element analysis only lie in $\mathcal{H}^1(\Omega)$. We therefore draw the basis functions, ϕ^a in Equations (6) and (7), from the family of Non-Uniform Rational B-Splines (NURBS), and adopt Isogeometric Analysis (IGA) in our simulations to find the solutions in $\mathcal{H}^2(\Omega)$. A discussion of the NURBS basis and IGA is beyond the scope of this communication; interested readers are directed to the original works on this topic, such as Ref. [37] and references therein.

2.5 Identification of basis operators via two stage stepwise regression

To identify a dynamical system, we need to generate all possible basis operators, χ_1 and χ_2 , acting on the solution, compute the non-zero coefficient for each basis operator that is in the model (active bases), while also attaining coefficients of zero for the basis operators that are not in the model (inactive bases). We begin by putting together the right hand-sides of Equations (29) and (30) at each time $\{\dots, t_{n-1}, t_n, t_{n+1}, \dots\}$. Let

$$\mathbf{y}_1 = \begin{bmatrix} \vdots \\ \frac{1}{\Delta t} \left(\frac{1}{V_{n-1}} \int_{\Omega_{n-1}} C_{n-1} dv - \frac{1}{V_{n-2}} \int_{\Omega_{n-2}} C_{n-2} dv \right) \\ \frac{1}{\Delta t} \left(\frac{1}{V_n} \int_{\Omega_n} C_n dv - \frac{1}{V_{n-1}} \int_{\Omega_{n-1}} C_{n-1} dv \right) \\ \frac{1}{\Delta t} \left(\frac{1}{V_{n+1}} \int_{\Omega_{n+1}} C_{n+1} dv - \frac{1}{V_n} \int_{\Omega_n} C_n dv \right) \\ \vdots \end{bmatrix} \quad (36)$$

and

$$\mathbf{y}_2 = \begin{bmatrix} \vdots \\ \frac{1}{2\Delta t} \left(\frac{1}{V_{n-1}} \int_{\Omega_{n-1}} C_{n-1}^2 dv - \frac{1}{V_{n-2}} \int_{\Omega_{n-2}} C_{n-2}^2 dv \right) - \frac{1}{V_{n-1}} \int_{\Omega_{n-1}} C \chi_1 dv \cdot \boldsymbol{\theta}_1 \\ \frac{1}{2\Delta t} \left(\frac{1}{V_n} \int_{\Omega_n} C_n^2 dv - \frac{1}{V_{n-1}} \int_{\Omega_{n-1}} C_{n-1}^2 dv \right) - \frac{1}{V_n} \int_{\Omega_n} C \chi_1 dv \cdot \boldsymbol{\theta}_1 \\ \frac{1}{2\Delta t} \left(\frac{1}{V_{n+1}} \int_{\Omega_{n+1}} C_{n+1}^2 dv - \frac{1}{V_n} \int_{\Omega_n} C_n^2 dv \right) - \frac{1}{V_{n+1}} \int_{\Omega_{n+1}} C \chi_1 dv \cdot \boldsymbol{\theta}_1 \\ \vdots \end{bmatrix} \quad (37)$$

be the target vectors formed as labels from the data at the two stages, respectively. Likewise, we form the respective matrices, Ξ_1 and Ξ_2 , containing all possible operator bases:

$$\Xi_1 = \begin{bmatrix} \vdots & \vdots & \vdots & \vdots \\ \frac{1}{V_{n-1}} \int_{\Omega_{n-1}} 1 dv & \frac{1}{V_{n-1}} \int_{\Omega_{n-1}} C_{n-1} dv & \frac{1}{V_{n-1}} \int_{\Omega_{n-1}} C_{n-1}^2 dv & \dots \\ \frac{1}{V_n} \int_{\Omega_n} 1 dv & \frac{1}{V_n} \int_{\Omega_n} C_n dv & \frac{1}{V_n} \int_{\Omega_n} C_n^2 dv & \dots \\ \frac{1}{V_{n+1}} \int_{\Omega_{n+1}} 1 dv & \frac{1}{V_{n+1}} \int_{\Omega_{n+1}} C_{n+1} dv & \frac{1}{V_{n+1}} \int_{\Omega_{n+1}} C_{n+1}^2 dv & \dots \\ \vdots & \vdots & \vdots & \vdots \end{bmatrix} \quad (38)$$

$$\Xi_2 = \begin{bmatrix} \vdots & \vdots & \vdots \\ \chi_{2_{n-1}}^{\nabla^2 C, C} & \chi_{2_{n-1}}^{\nabla^4 C, C} & \cdots \\ \chi_{2_n}^{\nabla^2 C, C} & \chi_{2_n}^{\nabla^4 C, C} & \cdots \\ \chi_{2_{n+1}}^{\nabla^2 C, C} & \chi_{2_{n+1}}^{\nabla^4 C, C} & \cdots \\ \vdots & \vdots & \vdots \end{bmatrix} \quad (39)$$

Then Equations (29) and (30) can be expressed as

$$\text{Stage 1:} \quad \mathbf{y}_1 = \Xi_1 \boldsymbol{\theta}_1 \quad (40)$$

and

$$\text{Stage 2:} \quad \mathbf{y}_2(\boldsymbol{\theta}_1) = \Xi_2 \boldsymbol{\theta}_2. \quad (41)$$

Equations (40) and (41) immediately deliver the two-stage algorithm of VSI, first for the coefficient vector $\boldsymbol{\theta}_1$, and then for $\boldsymbol{\theta}_2$ given the estimate of $\boldsymbol{\theta}_1$. Thus splitting the process into two stages also alleviates the curse of dimensionality as a smaller number of operators needs to be considered at each stage for parsimonious identification.

The coefficient vectors $\boldsymbol{\theta}_1$ and $\boldsymbol{\theta}_2$ in Equations (40) and (41) can be solved by minimizing the squared-norm loss functions l_1 and l_2 :

$$\boldsymbol{\theta}_1 = \arg \min_{\tilde{\boldsymbol{\theta}}_1} \left\{ l_1 := \left\| \mathbf{y}_1 - \Xi_1 \tilde{\boldsymbol{\theta}}_1 \right\|_2^2 \right\} \quad (42)$$

$$\boldsymbol{\theta}_2 = \arg \min_{\tilde{\boldsymbol{\theta}}_2} \left\{ l_2 := \left\| \mathbf{y}_2 - \Xi_2 \tilde{\boldsymbol{\theta}}_2 \right\|_2^2 \right\}, \quad (43)$$

which have analytical solutions expressible via the pseudo-inverses:

$$\boldsymbol{\theta}_1 = (\Xi_1^T \Xi_1)^{-1} \Xi_1^T \mathbf{y}_1 \quad (44)$$

$$\boldsymbol{\theta}_2 = (\Xi_2^T \Xi_2)^{-1} \Xi_2^T \mathbf{y}_2. \quad (45)$$

For robustness in the presence of noise and outliers, we use ridge regression to inject regularization. The optimization problems in Equations (42) and Equation (43) are then updated with additional penalty terms:

$$\boldsymbol{\theta}_1 = \arg \min_{\tilde{\boldsymbol{\theta}}_1} \left\{ l_1(\tilde{\boldsymbol{\theta}}_1) + \lambda_1 \left\| \tilde{\boldsymbol{\theta}}_1 \right\|_2^2 \right\} \quad (46)$$

$$\boldsymbol{\theta}_2 = \arg \min_{\tilde{\boldsymbol{\theta}}_2} \left\{ l_2(\tilde{\boldsymbol{\theta}}_2) + \lambda_2 \left\| \tilde{\boldsymbol{\theta}}_2 \right\|_2^2 \right\} \quad (47)$$

where λ_1 and λ_2 are regularization hyperparameters, with solutions

$$\boldsymbol{\theta}_1 = (\boldsymbol{\Xi}_1^T \boldsymbol{\Xi}_1 + \lambda_1 \mathbf{I})^{-1} \boldsymbol{\Xi}_1^T \mathbf{y}_1 \quad (48)$$

$$\boldsymbol{\theta}_2 = (\boldsymbol{\Xi}_2^T \boldsymbol{\Xi}_2 + \lambda_2 \mathbf{I})^{-1} \boldsymbol{\Xi}_2^T \mathbf{y}_2. \quad (49)$$

However, performing a standard, one-shot ridge regression for the full $\boldsymbol{\theta}$ vector will lead to a solution with nonzero contributions in all components of the vector. Such a solution of the system identification will be overfit to the data (and potentially to noise in the data), and lose parsimony by failing to sharply delineate the relevant bases. Another option is to use compressive sensing techniques [38, 39] that employ ℓ_1 -regularization, instead. However, we found their performance for system identification to be highly sensitive to the selection of regularization hyperparameters, leading to VSI results that are similar to one-shot ridge regression for $\boldsymbol{\theta}$. These observations then motivate us to take a different approach to iteratively eliminate the operators that have been identified to be inactive.

2.5.1 Stepwise regression

In this work, we use backward model selection by stepwise regression [40], which, as we have demonstrated, delivers parsimonious results with VSI [27]. The algorithm is summarized below.

Algorithm 1: Model selection by Stepwise regression:

Step 0: Establish target vector \mathbf{y} and matrix of bases $\boldsymbol{\Xi}$.

Step 1: Solve $\boldsymbol{\theta}^i$ by the linear regression problems, Equations (40) and (41), using ridge regression. Calculate the loss function at this iteration, l^i .

Step 2: Eliminate basis operators in matrix $\boldsymbol{\Xi}$ by deleting their columns, using the F -test introduced below. Set to zero the corresponding components of $\boldsymbol{\theta}^i$. GOTO Step 1. Note that at this stage the loss function remains small ($l^i \sim l^{i-1}$), and the solution may be overfit.

Step 3: The algorithm stops if the F -test does not allow elimination of any more basis operators. Beyond this, the loss function increases dramatically for any further reduction.

Starting from a dictionary containing all potential relevant operators and while the residual remains small, we eliminate the inactive operators iteratively until the model becomes underfit as indicated by a drastic increase of residual norm. Since the model at iteration i contains fewer bases than at iteration $i - 1$ and is therefore more restrictive, the loss function, in general, is higher at iteration i than at iteration $i - 1$. In this sense, model always becomes “worse” after eliminating

any basis. We want to determine whether the model at iteration i is significantly worse than at iteration $i - 1$. If so, the basis is not eliminated. There are several choices for the criterion for eliminating basis terms. Here, we adopt a widely used statistical criterion called the F -test, also used by us previously [27]. The significance of the change between the model at iterations i and $i - 1$ is evaluated by:

$$F = \frac{\frac{l^i - l^{i-1}}{p^{i-1} - p^i}}{\frac{l^{i-1}}{m - p^{i-1}}} \quad (50)$$

where p^i is the number of bases at iteration i and m is the total number of operator bases. Model selection is achieved through the following algorithm:

Algorithm 2: Model selection by the F -test:

Step 1:

Tentatively eliminate the basis corresponding to coefficients in θ^i which are smaller than the pre-defined threshold. Evaluate the F value followed by ridge regression on the reduced basis set.

Step 2:

IF $F < \alpha$

THEN formally eliminate these bases in matrix Ξ , by deleting the corresponding columns. GOTO Step 1.

ELSE GOTO Step 1, and choose another basis as a candidate for elimination.

In this work we adopt the threshold:

$$\text{threshold}^i = \hat{\theta}^i + \epsilon \quad (51)$$

$$\hat{\theta}^i = \arg \min_{\{\theta_\alpha^i\}_{\alpha=1}^m} |\theta_\alpha^i| \quad (52)$$

where, as defined in Equation (52) $\hat{\theta}^i$ is the component with the smallest magnitude in $\{\theta_\alpha^i\}_{\alpha=1}^m$, and ϵ is a small tolerance.^a The penalty coefficients in ridge regression, λ_1 and λ_2 , are chosen to lie in the range $[10^{-10}, 10^{-1}]$ by leave-one-out cross-validation at each iteration. The hyperparameter α is chosen to lie in the range $[1, 10]$, by five-fold cross validation. We summarize the stepwise regression algorithm and F -test in Figure 2.

2.6 Variational System Identification with dynamic data

We now use the framework detailed in the preceding section to identify the parabolic PDEs that govern pattern formation. To test our methods, we deploy them here to identify PDEs using data

^aThe F test serves a similar purpose as the Pareto analysis presented in [41] to select parsimonious governing equations from a large set of potential models.

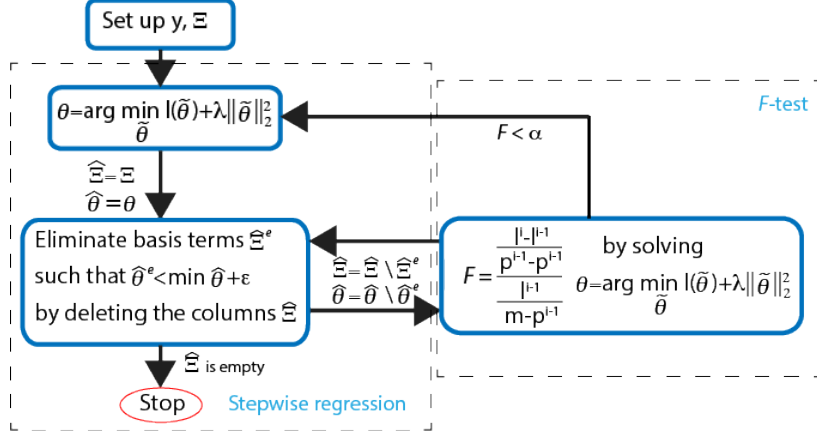


Figure 2: Schematic of the algorithms for stepwise regression and the F -test.

synthesized through high-fidelity, direct numerical simulations (DNS) from known “true-solution” systems detailed in Section 2.6.1. We consider test cases with the following two pattern formation models for data generation, with their true parameter values summarized in Table 1:

Model 1:

$$\frac{\partial C_1}{\partial t} = D_1 \nabla^2 C_1 + R_{10} + R_{11} C_1 + R_{13} C_1^2 C_2 \quad (53)$$

$$\frac{\partial C_2}{\partial t} = D_2 \nabla^2 C_2 + R_{20} + R_{21} C_1^2 C_2 \quad (54)$$

$$\text{with } \nabla C_1 \cdot \mathbf{n} = 0; \quad \nabla C_2 \cdot \mathbf{n} = 0 \text{ on } \Gamma \quad (55)$$

where Γ is the domain boundary. Model 1 represents the coupled diffusion-reaction equations for two species following Schnakenberg kinetics [42], but with different boundary conditions. For an activator-inhibitor species pair, these equations use auto-inhibition with cross-activation of a short range species, and auto-activation with cross-inhibition of a long range species to form so-called Turing patterns [5].

Model 2:

$$\frac{\partial C_1}{\partial t} = \nabla \cdot (M_1 \nabla \mu_1) \quad (56)$$

$$\frac{\partial C_2}{\partial t} = \nabla \cdot (M_2 \nabla \mu_2) \quad (57)$$

$$\mu_1 = \frac{\partial g}{\partial C_1} - k_1 \nabla^2 C_1 \quad (58)$$

$$\mu_2 = \frac{\partial g}{\partial C_2} - k_2 \nabla^2 C_2 \quad (59)$$

$$\text{with } \nabla \mu_1 \cdot \mathbf{n} = 0; \quad \nabla C_1 \cdot \mathbf{n} = 0 \text{ on } \Gamma \quad (60)$$

$$\nabla \mu_2 \cdot \mathbf{n} = 0; \quad \nabla C_2 \cdot \mathbf{n} = 0 \text{ on } \Gamma \quad (61)$$

where g is a non-convex, “homogeneous” free energy density function, whose form has been chosen from Ref. [14]:

$$\begin{aligned} g(C_1, C_2) = & \frac{3d}{2s^4} ((2C_1 - 1)^2 + (2C_2 - 1)^2)^2 + \frac{d}{s^3} (2C_2 - 1) ((2C_2 - 1)^2 - 3(2C_1 - 1)^2) \\ & - \frac{3d}{2s^2} ((2C_1 - 1)^2 + (2C_2 - 1)^2). \end{aligned} \quad (62)$$

Model 2 is a two-field Cahn-Hilliard system with fourth-order terms in the concentrations, C_1 and C_2 , which become apparent on substituting Equations (58) and (59) into (56) and (57), respectively. The three-well non-convex free energy density function (see Figure 3), $g(C_1, C_2)$, drives segregation of the system into two distinct phases. We have previously used this system to make connections with cell segregation in developmental biology [14]. The diffusion-reaction equations occur widely in the context of nucleation and growth phenomena in materials physics. The Cahn-Hilliard equation [4] also occupies a central role in the materials physics literature for modelling phase transformations developing from a uniform concentration field in the presence of a concentration instability.

D_1	D_2	R_{10}	R_{11}	R_{13}	R_{20}	R_{21}	M_1	M_2	k_1	k_2	d	s
1	40	0.1	-1	1	0.9	-1	0.1	0.1	10	10	0.4	0.7

Table 1: True parameter values used in DNS for synthesizing test data.

Substituting the parameter values from Table 1, we present the weak form of each model:

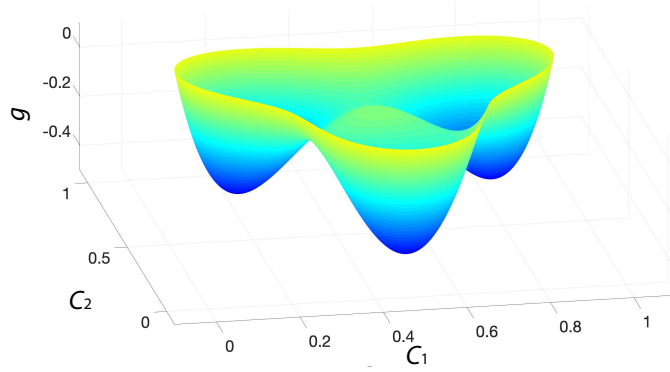


Figure 3: The three-well non-convex tissue energy density function.

Model 1:

$$\int_{\Omega} w_1 \frac{\partial C_1}{\partial t} dv = \int_{\Omega} -1 \nabla w_1 \cdot \nabla C_1 dv + \int_{\Omega} w_1 (0.1 - C_1 + 1C_1^2 C_2) dv \quad (63)$$

$$\int_{\Omega} w_2 \frac{\partial C_2}{\partial t} dv = \int_{\Omega} -40 \nabla w_2 \cdot \nabla C_2 dv + \int_{\Omega} w_2 (0.9 - 1C_1^2 C_2) dv \quad (64)$$

Model 2:

$$\begin{aligned} \int_{\Omega} w_1 \frac{\partial C_1}{\partial t} dv &= \int_{\Omega} \nabla w_1 \cdot (-17.8126 + 47.98C_1 + 21.591C_2 - 47.98C_1^2 - 15.9933C_2^2) \nabla C_1 dv \\ &+ \int_{\Omega} \nabla w_1 \cdot (-10.7955 + 21.591C_1 + 15.9933C_2 - 31.9867C_1C_2) \nabla C_2 dv \\ &+ \int_{\Omega} -1 \nabla^2 w_1 \nabla^2 C_1 dv \end{aligned} \quad (65)$$

$$\begin{aligned} \int_{\Omega} w_2 \frac{\partial C_2}{\partial t} dv &= \int_{\Omega} \nabla w_2 \cdot (-10.7955 + 21.591C_1 + 15.9933C_2 - 31.9867C_1C_2) \nabla C_1 dv \\ &+ \int_{\Omega} \nabla w_2 \cdot (-12.2149 + 15.9933C_1 + 42.3823C_2 - 15.9933C_1^2 - 47.98C_2^2) \nabla C_2 dv \\ &+ \int_{\Omega} -1 \nabla^2 w_2 \nabla^2 C_2 dv \end{aligned} \quad (66)$$

2.6.1 Data preparation

All computations have been implemented in the `mechanoChemIGA` code framework, a library for modeling mechano-chemical problems using isogeometric analytics, available at <https://github.com>.

com/mechanoChem/mechanoChem. The IBVPs presented here are two-dimensional. Data generation by direct numerical simulation was carried out on uniformly discretized 400×400 meshes. Adaptive time stepping is used^b with a direct solver. The initial conditions for all simulations are a constant value corrupted with random noise at each grid point:

$$C_{1,i} = 0.5 + \delta_{1,i} \quad (67)$$

$$C_{2,i} = 0.5 + \delta_{2,i} \quad (68)$$

where $\delta_{1,i}, \delta_{2,i} \sim \mathcal{U}(-0.01, 0.01)$ are independent (across i), uniform, random variables at each nodal mesh point i .

To mimic the experimental data that would be necessarily collected from multiple physical specimens due to the destructive nature of the acquisition procedure, we run each model for 30 different simulations, each with an independently and identically distributed (i.i.d.) realization of the initial condition in Equations (67) and (68) (e.g., see upper plots in Figure 4). The patterns generated from separate simulations, with initial conditions randomized as above, are non-identical but statistically similar (e.g., see lower plots in Figure 4). In this study we collected the data at 30 time steps, each over a spatially unrelated snapshot from a different simulation. Therefore, the total dataset of 30 snapshots does not correspond to a common initial condition or spatial subdomain.

The experimental data may also be noisy and of varying sparsity, often available only at low spatial resolution due to cost limitations or accessibility constraints of historical data. To mimic noisy data, we superpose the synthetic solutions C_1 and C_2 with an i.i.d. Gaussian noise $\mathcal{N}(0, \sigma^2)$ at each grid point. To simulate scenarios with different data sparsity, we use the full 400×400 domain as well as proportionally smaller subdomains of 300×300 , 200×200 , 100×100 and 50×50 meshes. These proper subsets represent incomplete data and, as discussed, could possibly come from spatially unrelated and even non-overlapping subdomains at different times. Note that while each snapshot consists of values from multiple grid points, a single snapshot yields only one “data point” due to the integration forms at the two stage of identification (See Equation (29) and (30)). Having clean and noisy snapshots at varying sparsity, from different simulations representing distinct specimens and unrelated, non-overlapping subdomains, we generate 34 candidate basis operators in addition to the time derivative terms, summarized in Table 2. The construction of operator basis in weak form is quite inexpensive, equivalent to the finite element assembly process (even when considering a large set of candidate operators). Furthermore, the bases only need to be constructed once in the entire VSI procedure, and the subsequent regression steps do not ever need them to be reconstructed; this is because the bases are constructed from data which are given and fixed. The computational expense of Stepwise regression is equal to $\sum_i^N t_i$ where N is the total iteration number and t_i is the expense of regression problem at the i th iteration. N increases

^bThe time step size lies in the range $\Delta t = [0.25, 2]$ depending on the convergence of the solver.

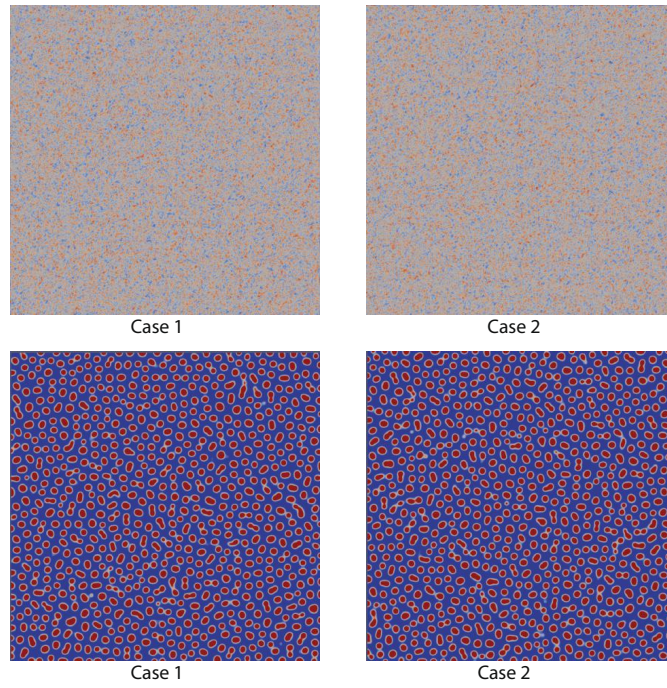


Figure 4: Upper plots: Concentration at $t = 0$ of two cases representing distinct experimental specimens. The perturbation is re-generated for every simulation. Lower plots: Concentration at $t = 20$. The Turing patterns generated from different initial conditions appear statistically similar.

linearly and t_i increases roughly quadratically, for iterative solvers, relative to the size of the basis that was considered. As a result, the total computational expense increases roughly cubically. For the problems considered in this communication, VSI generally takes only minutes on a personal laptop.

Table 2: Candidate basis operators for model selection. Asterisks, (*) in the left column represent algebraic operators on C_1 and C_2 .

Type of basis	Basis in weak form
$\nabla(*\nabla C_1)$	$\begin{array}{cccc} \int_{\Omega} \nabla w \nabla C_1 dv & \int_{\Omega} \nabla w C_1 \nabla C_1 dv & \int_{\Omega} \nabla w \nabla C_2 dv & \\ \int_{\Omega} \nabla w C_1^2 \nabla C_1 dv & \int_{\Omega} \nabla w C_1 C_2 \nabla C_1 dv & \int_{\Omega} \nabla w C_2^2 \nabla C_1 dv & \\ \int_{\Omega} \nabla w C_1^3 \nabla C_1 dv & \int_{\Omega} \nabla w C_1^2 C_2 \nabla C_1 dv & \int_{\Omega} \nabla w C_1 C_2^2 \nabla C_1 dv & \int_{\Omega} \nabla w C_2^3 \nabla C_1 dv \end{array}$
$\nabla(*\nabla C_2)$	$\begin{array}{cccc} \int_{\Omega} \nabla w \nabla C_2 dv & \int_{\Omega} \nabla w C_1 \nabla C_2 dv & \int_{\Omega} \nabla w \nabla C_2 dv & \\ \int_{\Omega} \nabla w C_1^2 \nabla C_2 dv & \int_{\Omega} \nabla w C_1 C_2 \nabla C_2 dv & \int_{\Omega} \nabla w C_2^2 \nabla C_2 dv & \\ \int_{\Omega} \nabla w C_1^3 \nabla C_2 dv & \int_{\Omega} \nabla w C_1^2 C_2 \nabla C_2 dv & \int_{\Omega} \nabla w C_1 C_2^2 \nabla C_2 dv & \int_{\Omega} \nabla w C_2^3 \nabla C_2 dv \end{array}$
$\nabla^2(*\nabla^2 C)$	$\begin{array}{cccc} \int_{\Omega} \nabla^2 w \nabla^2 C_1 dv & \int_{\Omega} \nabla^2 w C_1 \nabla^2 C_1 dv & \int_{\Omega} \nabla^2 w \nabla^2 C_2 dv & \int_{\Omega} \nabla^2 w C_2 \nabla^2 C_2 dv \end{array}$
non-gradient	$\begin{array}{cccc} -\int_{\Omega} w dv & -\int_{\Omega} w C_1 dv & -\int_{\Omega} w C_2 dv & \\ -\int_{\Omega} w C_1^2 dv & -\int_{\Omega} w C_1 C_2 dv & -\int_{\Omega} w C_2^2 dv & \\ -\int_{\Omega} w C_1^3 dv & -\int_{\Omega} w C_1^2 C_2 dv & -\int_{\Omega} w C_1 C_2^2 dv & -\int_{\Omega} w C_2^3 dv \end{array}$

2.6.2 Similarity between snapshots of data in pattern forming physics

The similarity between snapshots of data arises due to the random distribution of features/particles in the patterns. Before identifying the governing PDEs, we examine the validity of Equations (13) and (14) arrived at from assumptions in Section 2.2. We first evaluate the total flux over the boundaries of snapshots with different sizes as shown in Figure 5. As snapshot size increases, the total flux, scaled by its volume, vanishes. This validates the relation (13) in the limit of large snapshots.

The patterns formed by the diffusion-reaction system are shown in the lower plot in Figure 4. The “particles” representing high concentrations of one species, attain random distributions over the entire domain. Figure 6 shows the first and second powers of C_1 and C_2 evaluated using data with different sizes of snapshots from separate simulations. The random perturbation affects the local features of C_1 and C_2 ; however, with increasing size of snapshots their similarity becomes evident. Consequently powers of the composition evaluated using data from snapshots (30 different simulations are shown) converge to their values using full field data on the entire domain. Together they validate Relation (14). The statistics start to converge when snapshots are bigger than 50×50 , and show very low variance relative to the entire domain when the snapshot size exceeds 200×200 . The similarity between snapshots becomes more evident as the ratio of particle

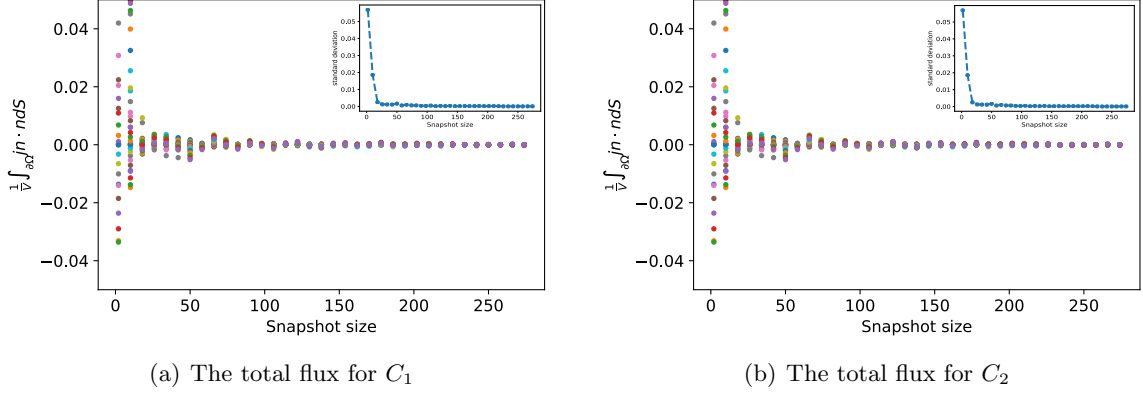


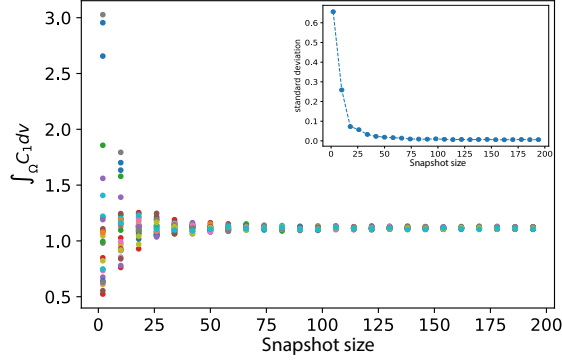
Figure 5: The total flux over snapshots of different sizes marked by different colors. The total flux converges to zero with increasing snapshot size. The embedded subplot shows the decreasing standard deviation.

spacing to the snapshots' linear dimension decreases (0.1 for the 50×50 snapshot to 0.025 for the 200×200 snapshot). The numerical validation of similarity between snapshots using Cahn-Hilliard and Allen-Cahn equations that govern the evolution of microstructure in materials are presented in the Appendix (see Section A and Figures 17-20).

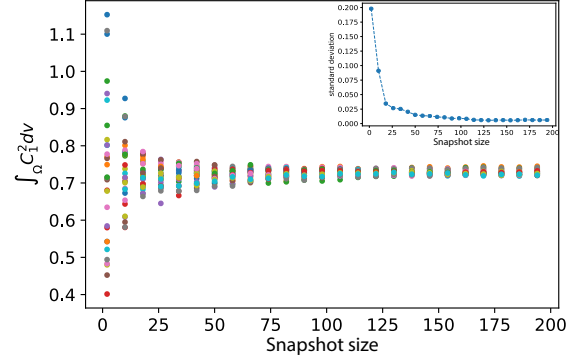
2.7 Numerical examples

The approximation of time derivatives needs data from at least two time steps, which are collected from different subdomains of the same simulation, or from simulations with different initial conditions, as discussed previously. Our first example uses noise-free data. Note however that since similarity is better satisfied between larger snapshots, an approximation error remains. Consequently the linear systems (Equations (40) and (41)) constructed by these noise-free data do not hold exactly. For instance Figure 7 shows the time derivatives constructed using data collected from different sizes of snapshots at each time step. Smaller snapshots yield high variance resulting from the initial condition's randomness (the only source of stochasticity, since we are utilizing noise-free data in this example), especially at later times. This is because variations with time are small when the dynamical system is close to steady state, and are easily dominated by the variance induced by initial conditions. Their poor representation challenges system identification, as we will discuss below.

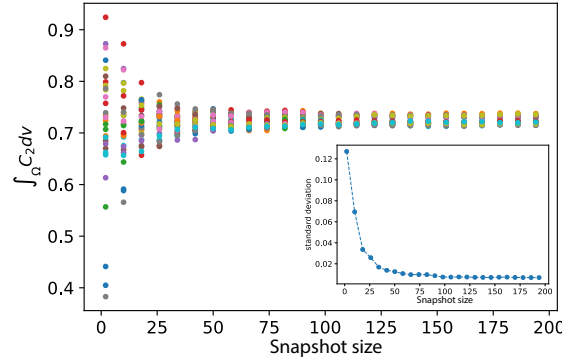
We successfully identified the algebraic operators in the governing equation for C_1 in Stage 1, as shown in Figure 8. The stem and leaf plots (left panel) show the coefficient of each operator scaled by its true value. The loss remains small until it converges (right panel) (i.e., when the loss significantly increases over an iteration). VSI using data collected from larger snapshots yields



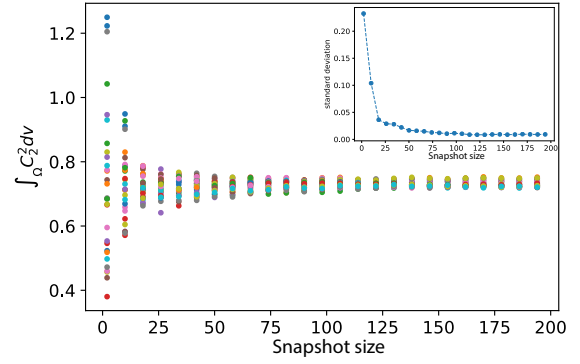
(a) First power of C_1



(b) Second power of C_1



(c) First power of C_2



(d) Second power of C_2

Figure 6: The powers evaluated using data generated by Model 1 from 30 simulations, marked by different colors, with different randomized initial conditions modeling data from different specimens. The embedded subplot shows the decreasing standard deviation of moments. Note the convergence with increasing snapshot size in the main and sub-plot.

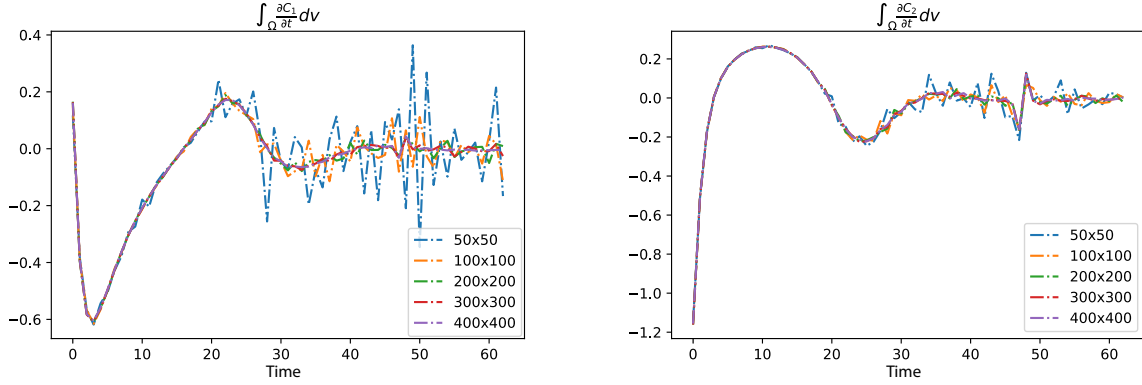


Figure 7: Time evolution of $\int_{\Omega} \frac{\partial C_1}{\partial t} dv$ and $\int_{\Omega} \frac{\partial C_2}{\partial t} dv$. Time derivatives constructed from small snapshots show higher variance due to initial conditions close to steady state.

lower losses, which also increase more dramatically compared to results using smaller snapshots, when an active operator is eliminated by trial in the stepwise regression process. In Stage 2 we successfully identified the one gradient dependent operator in the governing equation shown in Figure 9. We notice that in Stage 1 the gradually increasing loss function using data collected from small snapshots (50×50 mesh) allows a relatively small threshold in the F -test ($\alpha \sim 1$) to distinguish active and inactive operators. On the other hand, in Stage 2 the loss functions increase by half an order of magnitude in the last few iterations for the 100×100 and 50×50 cases, thus needing a higher F -test threshold ($\alpha \sim 10$) to distinguish inactive operators. These changes in loss function trajectories present a challenge in selecting α for the F -test, which must be tested via cross validation to balance model complexity and accuracy.

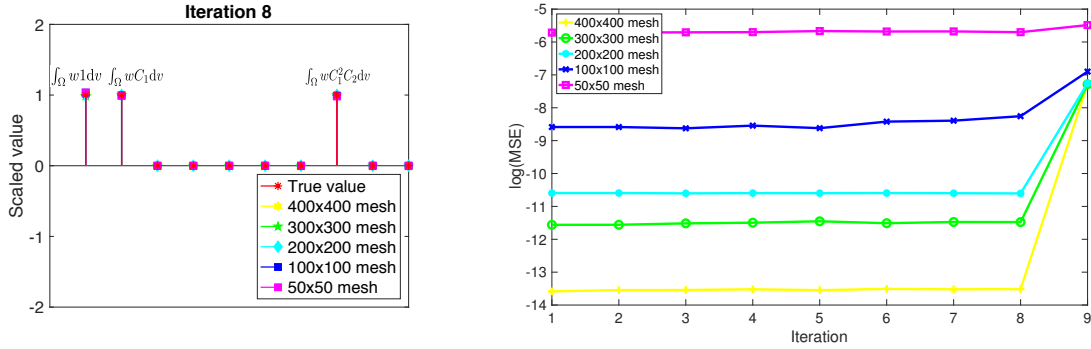


Figure 8: Inferred operators for C_1 from Stage 1 (left panel), and the loss (right panel) at each iteration using data generated from Model 1. The identified coefficients of active operators are scaled by their true values. The algorithm converges at iteration 8, beyond which the loss increases dramatically if any more operators are eliminated.

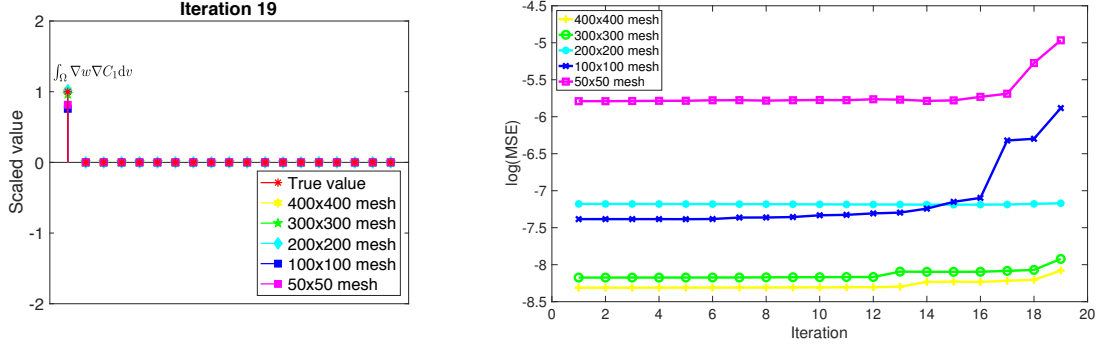


Figure 9: Inferred operators for C_1 from Stage 2 (left panel), and the loss (right panel) at each iteration using data generated from Model 1. The identified coefficients of active operators are scaled by their true values. The algorithm converges at iteration 19 with only one operator remaining.

We also successfully identified the algebraic operators in the governing equation for C_2 . However using the 50×50 and 100×100 dataset, the sparsity of data leads to the active Laplacian operator being wrongly eliminated. Note that the only surviving operators with these smaller snapshots are different than those identified from the larger snapshot datasets. With the 200×200 and larger snapshots, the Laplacian operator is correctly identified as the sole active operator. The full set of VSI results using noise-free data generated from Model 1 is summarized in Table 3.

mesh size	results
400×400	$\int_{\Omega} w_1 \frac{\partial C_1}{\partial t} dv = \int_{\Omega} -1.0252 \nabla w_1 \cdot \nabla C_1 dv + \int_{\Omega} w_1 (0.1 - 0.9996 C_1 + 0.9994 C_1^2 C_2) dv$ $\int_{\Omega} w_2 \frac{\partial C_2}{\partial t} dv = \int_{\Omega} -42.0655 \nabla w_2 \cdot \nabla C_2 dv + \int_{\Omega} w_2 (0.8998 - 0.9997 C_1^2 C_2) dv$
300×300	$\int_{\Omega} w_1 \frac{\partial C_1}{\partial t} dv = \int_{\Omega} -0.9644 \nabla w_1 \cdot \nabla C_1 dv + \int_{\Omega} w_1 (0.0987 - 0.9007 C_1 + 1.0009 C_1^2 C_2) dv$ $\int_{\Omega} w_2 \frac{\partial C_2}{\partial t} dv = \int_{\Omega} -42.2344 \nabla w_2 \cdot \nabla C_2 dv + \int_{\Omega} w_2 (0.89982 - 0.9998 C_1^2 C_2) dv$
200×200	$\int_{\Omega} w_1 \frac{\partial C_1}{\partial t} dv = \int_{\Omega} -1.0212 \nabla w_1 \cdot \nabla C_1 dv + \int_{\Omega} w_1 (0.0993 - 1.0007 C_1 + 1.0017 C_1^2 C_2) dv$ $\int_{\Omega} w_2 \frac{\partial C_2}{\partial t} dv = \int_{\Omega} -42.1083 \nabla w_2 \cdot \nabla C_2 dv + \int_{\Omega} w_2 (0.9001 - 0.9993 C_1^2 C_2) dv$
100×100	$\int_{\Omega} w_1 \frac{\partial C_1}{\partial t} dv = \int_{\Omega} -0.7576 \nabla w_1 \cdot \nabla C_1 dv + \int_{\Omega} w_1 (0.1035 - 0.9954 C_1 + 0.9908 C_1^2 C_2) dv$ $\int_{\Omega} w_2 \frac{\partial C_2}{\partial t} dv = \int_{\Omega} 2.77 \nabla w_2 \cdot C_1^2 \nabla C_1 dv + \int_{\Omega} w_2 (0.8982 - 0.9975 C_1^2 C_2) dv$
50×50	$\int_{\Omega} w_1 \frac{\partial C_1}{\partial t} dv = \int_{\Omega} -0.8154 \nabla w_1 \cdot \nabla C_1 dv + \int_{\Omega} w_1 (0.1035 - 0.9889 C_1 + 0.9804 C_1^2 C_2) dv$ $\int_{\Omega} w_2 \frac{\partial C_2}{\partial t} dv = \int_{\Omega} 3.91 \nabla w_2 \cdot C_1^2 C_2 \nabla C_1 dv + \int_{\Omega} w_2 (0.8896 - 0.9886 C_1^2 C_2) dv$

Table 3: Results using noise-free dynamic data generated from Model 1.

Next, we superimpose a Gaussian noise with zero mean and standard deviation $\sigma = 0.01$ over the data generated from Model 1. The noise on C_1 and C_2 gets amplified in the time derivative and spatial gradients. As shown in Figure 10, the noise dominates the true value of the Laplacian $\nabla^2 C_1$. The amplification of noise in the differential operators can cause failure of VSI that works with full-field data, as shown by Wang et al. [27]. However due to the integral nature of the first and second powers in the two stage VSI presented in this work, the noise is smoothed out. The zero mean ensures that the operators constructed with specific weighting functions are insensitive

to noise.

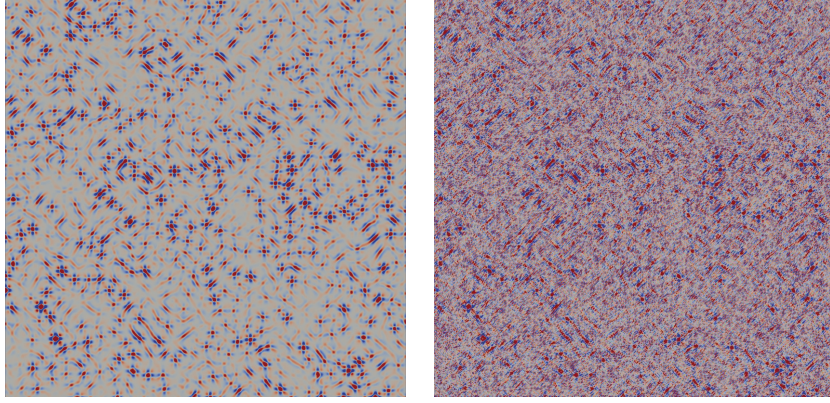


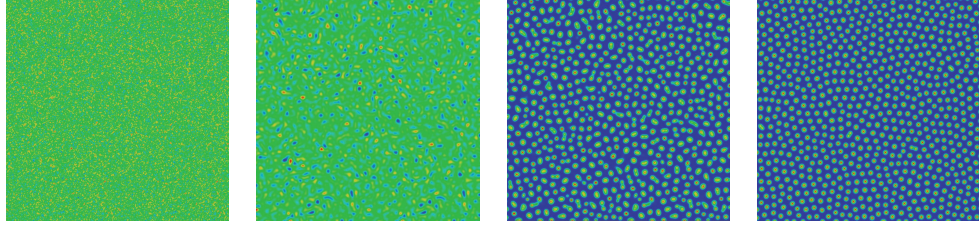
Figure 10: Noise-free (left) and noisy (right) fields of $\nabla^2 C_1$.

The full set of VSI results using noisy data generated from Model 1 are summarized in Table 4. We successfully identified the governing equations of C_1 . However there remain errors in the coefficients of the identified operators. For the governing equation of C_2 , all algebraic operators are successfully identified using noisy data. The single active differential operator, the Laplacian, is wrongly identified using smaller snapshots (200×200 , 100×100 and 50×50 datasets), while the larger snapshots allow its correct identification.

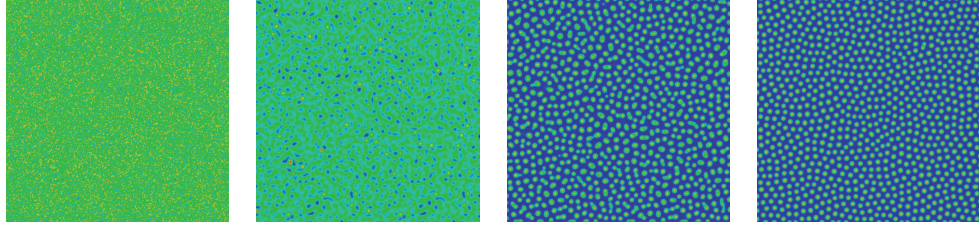
mesh size	results
400×400	$\int_{\Omega} w_1 \frac{\partial C_1}{\partial t} dv = \int_{\Omega} -1.0675 \nabla w_1 \cdot \nabla C_1 dv + \int_{\Omega} w_1 (0.0937 - 0.9876 C_1 + 0.9912 C_1^2 C_2) dv$ $\int_{\Omega} w_2 \frac{\partial C_2}{\partial t} dv = \int_{\Omega} -42.2038 \nabla w_2 \cdot \nabla C_2 dv + \int_{\Omega} w_2 (0.8662 - 0.9661 C_1^2 C_2) dv$
300×300	$\int_{\Omega} w_1 \frac{\partial C_1}{\partial t} dv = \int_{\Omega} -1.1105 \nabla w_1 \cdot \nabla C_1 dv + \int_{\Omega} w_1 (0.0941 - 0.9876 C_1 + 0.991 C_1^2 C_2) dv$ $\int_{\Omega} w_2 \frac{\partial C_2}{\partial t} dv = \int_{\Omega} -42.0852 \nabla w_2 \cdot \nabla C_2 dv + \int_{\Omega} w_2 (0.8668 - 0.9663 C_1^2 C_2) dv$
200×200	$\int_{\Omega} w_1 \frac{\partial C_1}{\partial t} dv = \int_{\Omega} -1.2102 \nabla w_1 \cdot \nabla C_1 dv + \int_{\Omega} w_1 (0.0944 - 0.9882 C_1 + 0.9912 C_1^2 C_2) dv$ $\int_{\Omega} w_2 \frac{\partial C_2}{\partial t} dv = \int_{\Omega} -55.257 \nabla w_2 \cdot \nabla C_2 dv + \int_{\Omega} w_2 (0.8662 - 0.9651 C_1^2 C_2) dv$
100×100	$\int_{\Omega} w_1 \frac{\partial C_1}{\partial t} dv = \int_{\Omega} -1.1579 \nabla w_1 \cdot \nabla C_1 dv + \int_{\Omega} w_1 (0.0895 - 0.9897 C_1 + 0.9992 C_1^2 C_2) dv$ $\int_{\Omega} w_2 \frac{\partial C_2}{\partial t} dv = \int_{\Omega} -54.989 \nabla w_2 \cdot \nabla C_2 dv + \int_{\Omega} w_2 (-0.8682 - 0.967 C_1^2 C_2) dv$
50×50	$\int_{\Omega} w_1 \frac{\partial C_1}{\partial t} dv = \int_{\Omega} -0.8997 \nabla w_1 \cdot \nabla C_1 dv + \int_{\Omega} w_1 (0.0836 - 0.9826 C_1 + 0.9973 C_1^2 C_2) dv$ $\int_{\Omega} w_2 \frac{\partial C_2}{\partial t} dv = \int_{\Omega} 7.93 \nabla w_2 \cdot \nabla C_2 dv + \int_{\Omega} w_2 (-0.8733 - 0.9726 C_1^2 C_2) dv$

Table 4: Results using noisy dynamic data generated from Model 1.

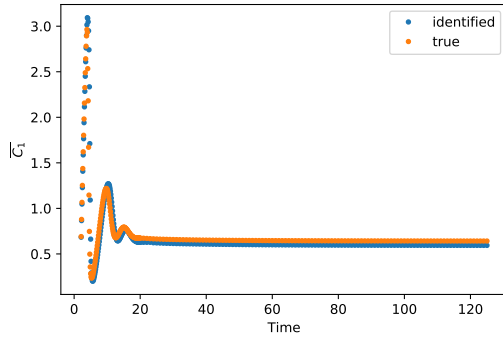
We chose the identified model using noisy data collected at 100×100 snapshot for comparison with the true model by solving with the same initial condition. The chosen identified model has the correctly identified operators but with the worst inference of the coefficients over the snapshots considered. Though the identified model yields a slightly sparser distribution of the particles due to the higher diffusivities (upper plots in Figure 11), it produces patterns that are similar to those in the true model in term of first and second powers (lower plots in Figure 11).



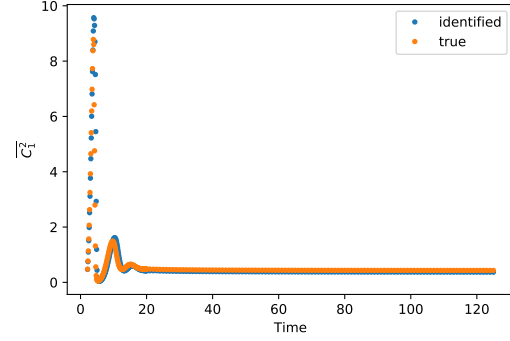
(a) C_1 concentration: identified Model 1



(b) C_1 concentration: true Model 1



(c) First power



(d) Second power

Figure 11: Comparison of the C_1 concentration field simulated by Model 1 inferred by VSI (a), against the true Model 1 (b). The results are shown at $t = 0, 5, 20, 100$. The good agreement for the first and second powers indicates the similarity between the identified model and the true model.

Unlike the diffusion-reaction system, Model 2, represented by Cahn-Hilliard equations, is conservative. Consequently the time derivative of the first power vanishes: $\frac{d}{dt} \int_{\Omega} C_n dv = 0$. The second moment, as well as other weak forms of algebraic and differential operators with $w^h = 1$ and $w^h = C^h$ also evolve very slowly after the initial regime of spinodal decomposition. With limited dynamic data, identifying the Cahn-Hilliard equations is challenging using the two stage VSI. We next present an alternate approach that leverages the data at steady state to successfully identify both diffusion-reaction and Cahn-Hilliard systems.

3 Variational System Identification with dynamic and steady state data

One challenge of the two-stage procedure introduced in Section 2 is data availability, where experimental measurements from the dynamic regime (non-steady state) of the system can be especially difficult and expensive to obtain. While the regression problems in Equations (40) and (41) generally require over-determined systems to arrive at good solutions, this consequently demands a large dataset to delineate the relevant bases, since the number of rows in Equations (40) and (41) is the number of time instants minus one. The challenge posed by spatially unrelated data and sparse time instants led us to the two-stage formulation of the problem with integral forms as presented above in Section 2.3. This treatment, however, sacrifices any high spatial resolution available in the experimental snapshots. As a remedy, we have developed an approach that leverages data with high spatial resolution at steady state (or near-steady state). With this new approach, it is possible to first identify all the operators up to a scaling factor, which can subsequently be determined by the dynamics. Inference of this scaling factor, controlled by the dynamics, can then be achieved using only one of the two stages described previously for the algebraic and differential operators. The essence of the VSI approach, namely, the treatment of equations in weak form, remains unchanged.

3.1 Variational System Identification of basis operators with steady state data

Data with high spatial resolution at steady state, or near-steady state, is typically obtained from modern microscopy methods. In fact the data satisfying the steady state equation:

$$\chi \cdot \theta = 0, \quad (69)$$

already provide rich information about the spatial operators (that is, other than time derivatives) in the system. By choosing a nontrivial χ_1 to be the target operator, the equation can be rewritten as:

$$-\chi_1 = \frac{1}{\theta_1} \bar{\chi} \cdot \bar{\theta}, \quad (70)$$

where $\bar{\chi} = \chi \setminus \{\chi_1\}$ and $\bar{\theta} = \theta \setminus \{\theta_1\}$. We are able to identify the coefficients, $\bar{\theta}$, up to a scaling constant, θ_1 , using the data at steady state by VSI [27]. However, in the absence of prior knowledge about the system, it may be the case that the selected target operator, χ_1 , is actually inactive (i.e., its prefactor $\theta_1 = 0$). Then Equation (70) is not valid for the data. Under such conditions, VSI will fail at parsimonious representation over the operators included in $\bar{\chi}$. “False” outcomes can then be detected by inconsistencies in the system identification, as we elaborate via examples below.

On the other hand, if in two (or more) trials distinct operators are chosen as targets, and if these chosen targets are all indeed active in the true system, then the same set $\bar{\chi}$ will be identified in these different trials with coefficients $\bar{\theta}$ differing only by a scaling factor. This consistency, up to a scaling factor, provides a confirmation test for VSI of the spatial operators with (near-)steady state data without the need for prior knowledge.

Nevertheless, when confronted with data on systems that are governed by multiple equations, the above approach to identify consistent sets of active operators via the confirmation test can break down. In particular, this can happen if one of the equations has only one operator that is distinct from those appearing in other equations governing the system, and its remaining operators number fewer than in any other equation of the system. In such a situation, the stepwise regression algorithm will detect the steady state equation with the greater number of operators as the only consistent set passing the confirmation test. Even the choice of the one distinct operator in the remaining equation as target operator will not pass the confirmation test for consistency (since upon looking for consistency, the equation with greater number of operators will be identified as it provides a feasible solution with lower loss). Our approach to this detection of only the lower loss solution is to deliberately suppress an operator in a consistent set that passes the confirmation test. This forces the stepwise regression algorithm to detect the equation with fewer operators, provided the suppressed operator is indeed inactive in this set. Subsequent consistency checks with the correctly suppressed operator will pass the confirmation test. The combined confirmation test for consistency with operator suppression appears as Algorithm 3.

Algorithm 3: Confirmation Test of Consistency with Operator Suppression:

Let $N_\chi := \#\chi$ (where $\#$ denotes cardinality) and $N_{\text{field}} :=$ number of unknown fields in data (e.g., for data on C_1, C_2 , $N_{\text{field}} = 2$)

Function: Test of Consistency

```

  FOR  $i = 1, \dots, N_\chi$ 
    With  $\chi_i$  as target vector, do stepwise regression to identify coefficients
     $\vartheta_i \in \mathbb{R}^{N_\chi-1}$ .
    IF  $i \geq 2$  &&  $\vartheta_i = \alpha \vartheta_j$  for  $j < i$  THEN
      Confirmation Test:  $\vartheta_i$  and  $\vartheta_j$  represent the same consistent set
    ELSE
       $\vartheta_i$  is inconsistent
    Collect all linearly independent consistent coefficient sets expressible as
     $\theta_\alpha \vartheta_\alpha, \theta_\beta \vartheta_\beta, \dots$  for  $\alpha, \beta, \dots \in \{1, \dots, N_\chi\}$ .

  While (True):
    Call Test of Consistency.
    IF  $\#\{\alpha, \beta, \dots\} < N_{\text{field}}$ 
      FOR  $i \in \{\alpha, \beta, \dots\}$ 
        Define  $\hat{\chi}_k$  to be the operator with coefficient  $\theta_{i_k}$  in  $\vartheta_i = \{\dots, \theta_{i_k}, \dots\}$ .
      Call Test of Consistency with  $\chi \setminus \hat{\chi}_k$ .
    ELSE
      EXIT

```

Thereafter, there remains only one unknown in the governing equations, which is the scaling factor, θ_1 :

$$\frac{\partial C}{\partial t} - \theta_1(\chi \cdot \theta) = 0, \quad (71)$$

which then can be identified using dynamic data and one of the two stages of VSI detailed in Sections 2.3–2.5. If an algebraic/differential operator was identified via Algorithm 3 for the (near-) steady state data, Stage 1/Stage 2 can be used respectively (Section 2.3). This is elaborated with examples in Section 3.2, and proves to be a powerful feature in favor of robustness and consistency of VSI for steady and dynamic data.

3.2 Numerical examples with steady state and dynamic data

The steady state form of Model 1 in strong form is:

$$D_1 \nabla^2 C_1 + R_{10} + R_{11} C_1 + R_{13} C_1^2 C_2 = 0 \quad (72)$$

$$D_2 \nabla^2 C_2 + R_{20} + R_{21} C_1^2 C_2 = 0. \quad (73)$$

Given steady state, or near-steady state data, such as for full field or snapshots of diffusion-reaction systems, VSI can identify the steady state governing equations using the Confirmation Test of Consistency with Operator Suppression in Algorithm 3. As discussed in Section 3.1, choosing inactive operators to be targets yields inconsistent results. Figure 12 shows that if two different (inactive) operators, $\int_{\Omega} \nabla w \cdot C_1 \nabla C_1 dv$ and $\int_{\Omega} \nabla w \cdot C_2 \nabla C_1 dv$ (in weak form), are chosen as targets, the identified results are completely different. The set of identified operators with $\int_{\Omega} \nabla w \cdot C_1 \nabla C_1 dv$ as target contains $\int_{\Omega} \nabla w \cdot C_2 \nabla C_1 dv$ but not *vice versa*. This is because choosing an inactive operator as the target removes it from the stepwise regression and model selection procedures in Algorithms 1 and 2, meaning that it has to be included in the identified set. Consequently, the identified sets of operators do not form a group of governing PDEs that models meaningful physics. This is reflected in the inconsistency between the operator sets.

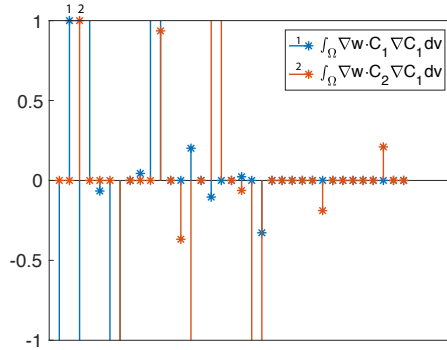


Figure 12: One example of inconsistently inferred operators with different targets using data at steady state. Choosing $\int_{\Omega} \nabla w \cdot C_1 \nabla C_1 dv$, labelled by 1, as target operator leads to a set of operators being identified, shown by the blue stems and leaves. This includes the operator $\int_{\Omega} \nabla w \cdot C_2 \nabla C_1 dv$ labelled by 2. However, choosing the latter as the target operator yields a different active set, shown as the orange stems and leaves. Both target operators are actually inactive, leading to inconsistency between the respective sets.

On the other hand, choosing the active operators as the targets does yield consistent identification. The plot on the left in Figure 13 shows that the identified set is consistent up to a scaling factor, with four different operators as, shown in the legend, as targets. This set identifies

the steady state equation (72). Note that the weak form operators $\int_{\Omega} w dv$ and $\int_{\Omega} w C_1 C_2^2 dv$ are common to Equations (72) and (73), but choosing either as target only yields the consistent set in Equation (72); i.e., the one with more operators, because this set leads to a lower loss. Suppression of either of the identified active operators $\int_{\Omega} \nabla w \cdot \nabla C_1 dv$ or $\int_{\Omega} w C_1 dv$, yields another set of consistent inferred operators, shown in the legend on the right in Figure 13. This set identifies the steady state equation for C_2 . This is a manifestation of the Confirmation Test of Consistency with Operator Suppression in Algorithm 3.

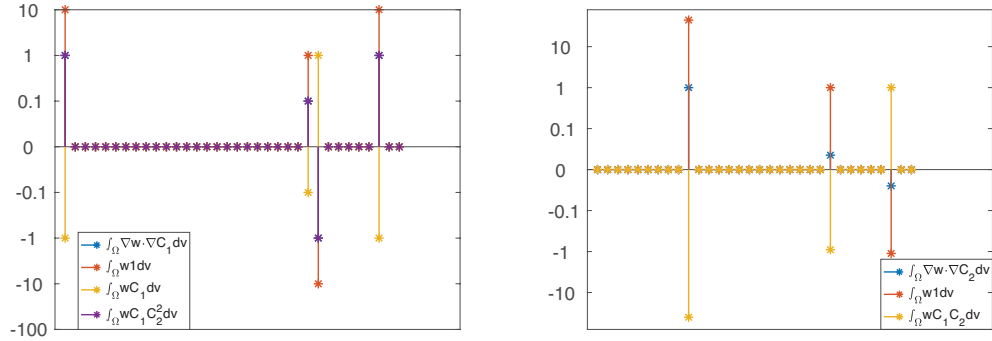


Figure 13: Two sets (left and right) of consistently inferred operators with different targets using data generated from Model 1 at steady state. The coefficient values have been plotted on the logarithmic scale in order to make them discernible across orders of magnitude. Each set consists of the operators in the legend of the corresponding sub-plot and is consistent up to a scaling factor. Note that the second set of consistently inferred operators is obtained on a reduced library of candidate operators without $\int_{\Omega} \nabla w \cdot \nabla C_1 dv$ or $\int_{\Omega} w C_1 dv$, the two operators in the first set of consistent inferred operators. The two sets, left and right, are the steady state equations for C_1 and C_2 in Equations (72) and (73), respectively.

In the following we choose the two Laplacian operators, $\nabla^2 C_1$ and $\nabla^2 C_2$, as targets and infer the remaining operators, $\bar{\chi}$:

$$\nabla^2 C_1 = \frac{1}{\theta_{D_1}} \bar{\chi} \cdot \bar{\theta} \quad (74)$$

$$\nabla^2 C_2 = \frac{1}{\theta_{D_2}} \bar{\chi} \cdot \bar{\theta}. \quad (75)$$

Without noise, very accurate results are obtained even with small snapshots. Next, using Stage 2 of the VSI approach, i.e. by choosing the weighting function to be $w^h = C_1^h$ and $w^h = C_2^h$, the diffusion coefficients θ_{D_1} and θ_{D_2} in Equations (74) and (75) are correctly identified. The final identified system using both steady state and dynamic data generated from Model 1 is shown in Table 5. Recall that the diffusion coefficients are not identifiable from early time data collected

with small snapshots as discussed before (see Table 3, where this failure was cast in terms of the Laplacian operator). However, they are identified using the Confirmation Test of Consistency with Operator Suppression (Algorithm 3) in combination with Stage 2 of the VSI approach (Algorithms 1 and 2).

mesh size	results
400×400	$\int_{\Omega} w_1 \frac{\partial C_1}{\partial t} dv = \int_{\Omega} -0.9998 \nabla w_1 \cdot \nabla C_1 dv + \int_{\Omega} w_1 (0.1 - 0.9998 C_1 + 0.9998 C_1^2 C_2) dv$ $\int_{\Omega} w_2 \frac{\partial C_2}{\partial t} dv = \int_{\Omega} -39.95 \nabla w_2 \cdot \nabla C_2 + \int_{\Omega} w_2 (0.8989 - 0.9987 C_1^2 C_2) dv$
300×300	$\int_{\Omega} w_1 \frac{\partial C_1}{\partial t} dv = \int_{\Omega} -1.001 \nabla w_1 \cdot \nabla C_1 dv + \int_{\Omega} w_1 (0.1 - 0.9998 C_1 + 0.9998 C_1^2 C_2) dv$ $\int_{\Omega} w_2 \frac{\partial C_2}{\partial t} dv = \int_{\Omega} -40.01 \nabla w_2 \cdot \nabla C_2 + \int_{\Omega} w_2 (0.9002 - 1.0002 C_1^2 C_2) dv$
200×200	$\int_{\Omega} w_1 \frac{\partial C_1}{\partial t} dv = \int_{\Omega} -0.995 \nabla w_1 \cdot \nabla C_1 dv + \int_{\Omega} w_1 (0.1001 - 1.001 C_1 + 1.001 C_1^2 C_2) dv$ $\int_{\Omega} w_2 \frac{\partial C_2}{\partial t} dv = \int_{\Omega} -40.02 \nabla w_2 \cdot \nabla C_2 + \int_{\Omega} w_2 (0.9005 - 1.005 C_1^2 C_2) dv$
100×100	$\int_{\Omega} w_1 \frac{\partial C_1}{\partial t} dv = \int_{\Omega} -0.0994 \nabla w_1 \cdot \nabla C_1 dv + \int_{\Omega} w_1 (0.0995 - 0.995 C_1 + 0.995 C_1^2 C_2) dv$ $\int_{\Omega} w_2 \frac{\partial C_2}{\partial t} dv = \int_{\Omega} -39.72 \nabla w_2 \cdot \nabla C_2 + \int_{\Omega} w_2 (-0.8937 - 0.993 C_1^2 C_2) dv$
50×50	$\int_{\Omega} w_1 \frac{\partial C_1}{\partial t} dv = \int_{\Omega} -0.0994 \nabla w_1 \cdot \nabla C_1 dv + \int_{\Omega} w_1 (0.0994 - 0.994 C_1 + 0.994 C_1^2 C_2) dv$ $\int_{\Omega} w_2 \frac{\partial C_2}{\partial t} dv = \int_{\Omega} -39.23 \nabla w_2 \cdot \nabla C_2 + \int_{\Omega} w_2 (-0.8827 - 0.9807 C_1^2 C_2) dv$

Table 5: Results using steady state and dynamic data generated from Model 1.

Cahn-Hilliard equations behave differently from the diffusion-reaction equations in terms of how they attain steady state. The initial, fast, spinodal decomposition regime is followed by the slower Ostwald ripening mechanism, in which the larger particles grow slowly at the expense of smaller ones. As a result, following the initial spinodal decomposition, the evolution of concentrations is extremely slow (see Figure 14), and thus the system is at near-steady state:

$$\nabla \cdot (M_1 \nabla \mu_1) \approx 0 \quad (76)$$

$$\nabla \cdot (M_2 \nabla \mu_2) \approx 0 \quad (77)$$

We again find the sets of consistent operators using Algorithm 3, and they appear in Figure 15. Unlike the manner in which Algorithm 3 played out for the steady state diffusion-reaction equations, the choice of target operators that are common to both governing equations in the system does not result in convergence to a single set of operators. This is because the two equations in Model 2 have more than a single operator that is unique to each of them. When these are chosen as targets, Algorithm 3 correctly identifies two distinct sets of operators, each being self-consistent. These sets represent the two Cahn-Hilliard equations (76) and (77).

In the following we choose the two biharmonic operators, $\nabla^4 C_1$ and $\nabla^4 C_2$, as the targets and infer the remaining operators, $\bar{\chi}$:

$$\nabla^4 C_1 = \frac{1}{\theta_{k_1}} \bar{\chi} \cdot \bar{\theta} \quad (78)$$

$$\nabla^4 C_2 = \frac{1}{\theta_{k_2}} \bar{\chi} \cdot \bar{\theta}. \quad (79)$$

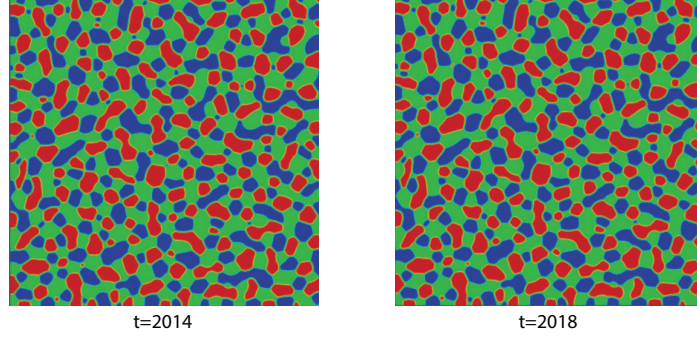


Figure 14: C_1 concentrations at closely spaced time instants with Model 2. The Cahn-Hilliard equations evolve very slowly in the Ostwald ripening stage following the initial, fast spinodal decomposition regime. The system is at near-steady state around $t = 2018$.

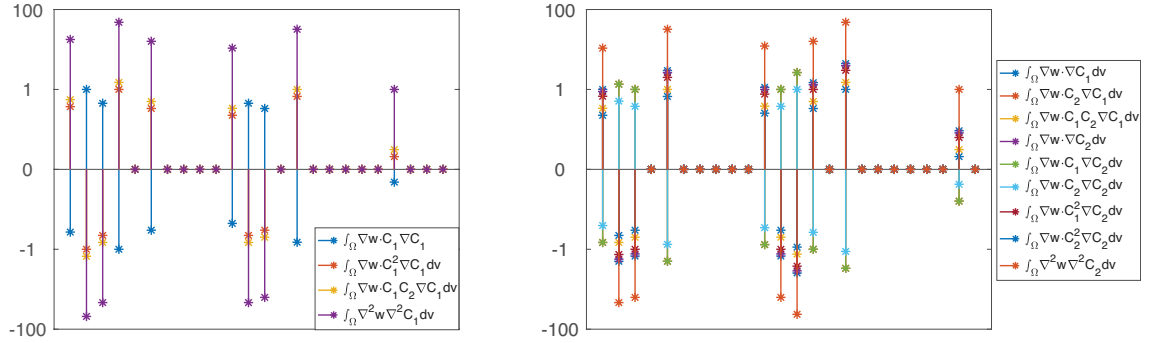


Figure 15: Two sets of consistently inferred operators starting with different targets and using data generated from Model 2 at steady state. The coefficient values have been plotted on the logarithmic scale in order to make them discernible across orders of magnitude. The two consistent sets consist of the operators, from left to right, appearing on the right hand-side of Equations (65) and (66), and differ only by a scaling factor. The two consistent sets are labelled by the target operator shown in the legends of the two sub-plots.

Very accurate results are obtained from data without noise, even if the snapshots are small. Following identification of the two consistent sets of operators at steady state by Algorithm 3, the scaling factors, θ_{k_1} and θ_{k_2} in Equations (78) and (79), i.e. the coefficients for biharmonic operators, are correctly identified using Stage 2 of VSI with dynamic data and weighting function $w^h = C_1^h$ and $w^h = C_2^h$. The final VSI results using both steady state and dynamic data generated from Model 2 are shown in Table 6.

mesh size	results
400 × 400	$\int_{\Omega} w_1 \frac{\partial C_1}{\partial t} dv = \int_{\Omega} \nabla w_1 \cdot (-17.417 + 46.9146C_1 + 21.114C_2 - 46.91C_1^2 - 15.64C_2^2) \nabla C_1 dv$ $+ \int_{\Omega} \nabla w_2 \nabla \cdot (-10.55 + 21.11C_1 + 15.64C_2 - 31.177C_1C_2) \nabla C_2 dv + \int_{\Omega} -0.978 \nabla^2 w_1 \nabla^2 C_1 dv$ $\int_{\Omega} w_2 \frac{\partial C_2}{\partial t} dv = \int_{\Omega} \nabla w_2 \cdot (-10.73 + 21.46C_1 + 15.9C_2 - 31.79C_1C_2) \nabla C_1 dv$ $+ \int_{\Omega} \nabla w_2 \nabla \cdot (-12.13 + 15.88C_1 + 42.12C_2 - 15.88C_1^2 - 47.68C_2^2) \nabla^2 C_2 dv + \int_{\Omega} -0.994 \nabla^2 w_2 \nabla^2 C_2 dv$
300 × 300	$\int_{\Omega} w_1 \frac{\partial C_1}{\partial t} dv = \int_{\Omega} \nabla w_1 \cdot (-15.992 + 43.08C_1 + 19.38C_2 - 43.08C_1^2 - 14.364C_2^2) \nabla C_1 dv$ $+ \int_{\Omega} \nabla w_2 \nabla \cdot (-9.69 + 19.38C_1 + 14.36C_2 - 28.71C_1C_2) \nabla C_2 dv + \int_{\Omega} -0.898 \nabla^2 w_1 \nabla^2 C_1 dv$ $\int_{\Omega} w_2 \frac{\partial C_2}{\partial t} dv = \int_{\Omega} \nabla w_2 \cdot (-9.82 + 19.65C_1 + 14.55C_2 - 29.11C_1C_2) \nabla C_1 dv$ $+ \int_{\Omega} \nabla w_2 \nabla \cdot (-11.11 + 14.54C_1 + 38.56C_2 - 14.54C_1^2 - 43.66C_2^2) \nabla^2 C_2 dv + \int_{\Omega} -0.91 \nabla^2 w_2 \nabla^2 C_2 dv$
200 × 200	$\int_{\Omega} w_1 \frac{\partial C_1}{\partial t} dv = \int_{\Omega} \nabla w_1 \cdot (-16.42 + 44.23C_1 + 19.9C_2 - 44.23C_1^2 - 14.74C_2^2) \nabla C_1 dv$ $+ \int_{\Omega} \nabla w_2 \nabla \cdot (-9.95 + 19.9C_1 + 14.74C_2 - 29.48C_1C_2) \nabla C_2 dv + \int_{\Omega} -0.86 \nabla^2 w_1 \nabla^2 C_1 dv$ $\int_{\Omega} w_2 \frac{\partial C_2}{\partial t} dv = \int_{\Omega} \nabla w_2 \cdot (-9.82 + 19.65C_1 + 14.55C_2 - 29.11C_1C_2) \nabla C_1 dv$ $+ \int_{\Omega} \nabla w_2 \nabla \cdot (-11.1 + 14.54C_1 + 38.56C_2 - 14.53C_1^2 - 43.66C_2^2) \nabla^2 C_2 dv + \int_{\Omega} -0.91 \nabla^2 w_2 \nabla^2 C_2 dv$
100 × 100	$\int_{\Omega} w_1 \frac{\partial C_1}{\partial t} dv = \int_{\Omega} \nabla w_1 \cdot (-15.31 + 41.25C_1 + 18.57C_2 - 41.25C_1^2 - 13.76C_2^2) \nabla C_1 dv$ $+ \int_{\Omega} \nabla w_2 \nabla \cdot (-9.27 + 18.55C_1 + 13.74C_2 - 27.48C_1C_2) \nabla C_2 dv + \int_{\Omega} -0.86 \nabla^2 w_1 \nabla^2 C_1 dv$ $\int_{\Omega} w_2 \frac{\partial C_2}{\partial t} dv = \int_{\Omega} \nabla w_2 \cdot (-11.66 + 23.32C_1 + 17.27C_2 - 34.55C_1C_2) \nabla C_1 dv$ $+ \int_{\Omega} \nabla w_2 \nabla \cdot (-13.18 + 17.24C_1 + 45.76C_2 - 17.24C_1^2 - 51.81C_2^2) \nabla^2 C_2 dv + \int_{\Omega} -1.08 \nabla^2 w_2 \nabla^2 C_2 dv$
50 × 50	$\int_{\Omega} w_1 \frac{\partial C_1}{\partial t} dv = \int_{\Omega} \nabla w_1 \cdot (-15.06 + 40.57C_1 + 18.28C_2 - 40.57C_1^2 - 13.55C_2^2) \nabla C_1 dv$ $+ \int_{\Omega} \nabla w_2 \nabla \cdot (-9.11 + 18.23C_1 + 13.5C_2 - 27C_1C_2) \nabla C_2 dv + \int_{\Omega} -0.846 \nabla^2 w_1 \nabla^2 C_1 dv$ $\int_{\Omega} w_2 \frac{\partial C_2}{\partial t} dv = \int_{\Omega} \nabla w_2 \cdot (-13.71 + 27.42C_1 + 20.31C_2 - 40.62C_1C_2) \nabla C_1 dv$ $+ \int_{\Omega} \nabla w_2 \nabla \cdot (-15.48 + 20.23C_1 + 53.81C_2 - 20.23C_1^2 - 60.94C_2^2) \nabla^2 C_2 dv + \int_{\Omega} -1.27 \nabla^2 w_2 \nabla^2 C_2 dv$

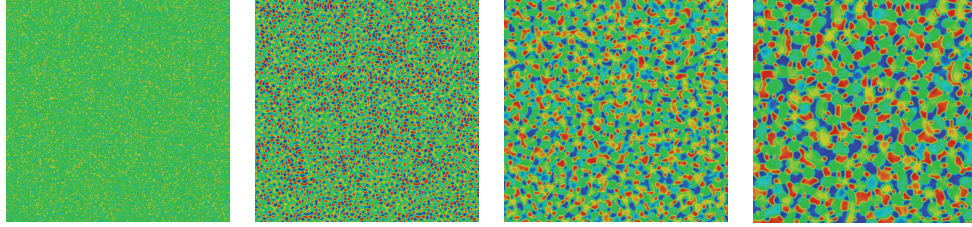
Table 6: Results using steady state and dynamic data generated from Model 2.

We remark that we have previously studied the effect of noise on VSI with full-field data [27]. Those results apply in entirety to VSI with steady state data as presented in this section.

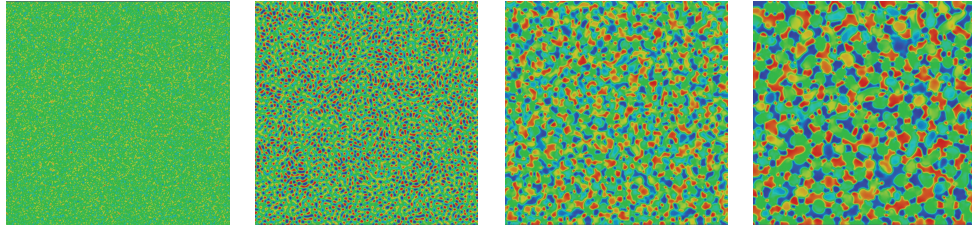
The identified model is compared with the true model by solving with same initial conditions (see Figure (16)). Although the results are different pointwise, being driven by the different kinetic coefficients that were inferred, the identified model produces similar patterns which are similar to the true model in terms of first and second powers of C_1 .

4 Discussion and conclusions

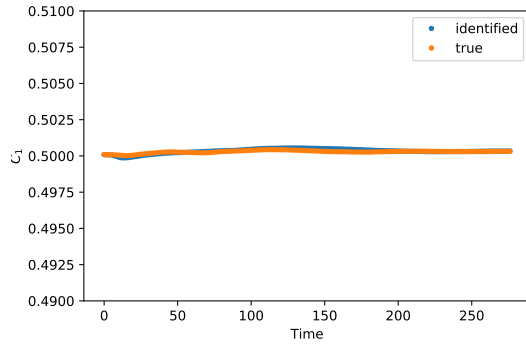
The development of patterns in many physical phenomena is governed by a range of spatio-temporal PDEs. It is compelling to attempt to discover the analytic forms of these PDEs from data, because doing so immediately provides insight to the governing physics. System identification has been explored using the strong form [26, 28, 29, 43, 44] and the weak form [27, 34, 35, 36] of the PDEs as discussed in the Introduction. These techniques, however all need data that are spatially overlapping



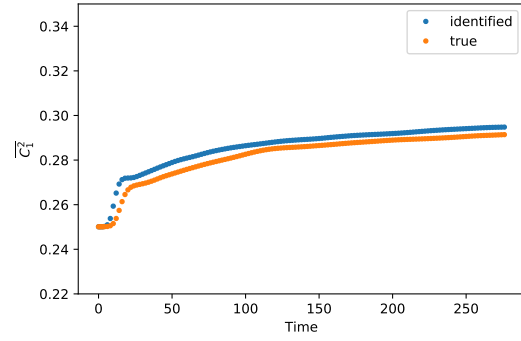
(a) C_1 concentration: identified Model 2



(b) C_1 concentration: true Model 2



(c) First power



(d) Second power

Figure 16: Comparison of the C_1 concentration field simulated by the identified Model 2 (a), against the true Model 2 (b). The results are shown at $t = 0, 10, 100, 276$. The results obtained from the identified model are similar to those obtained from the true model as shown by the good agreement between their first and second powers.

at distinct times in order to construct the time derivative operator. However, in materials physics in particular, the combination of processing and microscopy techniques results in datasets that are discordant with the PDE description of temporal evolution at fixed spatial locations. Microscopy data are only obtained over subsets of the entire domains, and the measured data at distinct times typically come from different experiments or specimens. This property of the datasets hinders the use of system identification methods including SINDy and VSI. While Bayesian methods, also discussed in the Introduction, are more flexible in working with such datasets, they require many forward solutions of the PDEs. Their computational expense makes it challenging to determine operators in PDEs from a comprehensive library of candidates.

For development of patterns in materials physics, dynamic information can be inferred from data collected from different specimens and at different times, because of the similarity of the patterns across snapshots (see Figures 1 and 4). Many quantitative features, e.g. the powers of the concentration fields, can be well approximated using such data. In the variational setting they can be recovered naturally by specific choices of weighting functions that allow a two-stage approach to separate the identification of algebraic and differential operators. VSI can thus be extended to incorporate spatially unrelated, non-overlapping and sparse information. Data available from larger snapshots; i.e., larger subsets of the entire domain yield better approximations of the global quantities as discussed in Section 2.6.2. The poor approximations using small snapshots pose challenges to system identification, resulting in inactive operators being incorrectly identified. This is particularly true for identification of operators that have much smaller contributions; e.g., operators with extremely small coefficients. In Appendix, we have shown how the VSI approach fares in this regime using dynamic data (see, Section B and Tables 8-10). In practice, however, we may have much higher resolution of data in experiments than the smallest snapshots of 50×50 that were assumed here. This opens a door to improving the success of our methods.

We had already shown [27] that, given data from a few temporal snapshots but with high spatial resolution, VSI can pinpoint the complete governing equations of dynamical systems. Here, we have further leveraged steady state data that already provide information about most of the operators in the system, up to scaling factors corresponding to kinetic coefficients such as diffusivities and mobilities that determine the time scales. In Section 3.2, we demonstrated that, using data at steady state, we could identify all the operators in the PDEs up to a scaling factor. Without prior knowledge it is challenging to choose relevant operators to be the targets in our methods at steady state. However, by examining the consistency of the inferred operators using different candidates as the target, we were able to identify all the governing equations at steady state. The associated Confirmation Test of Consistency with Operator Suppression has flavors of traditional approaches such as cross validation but is a mathematically stronger guarantee in that it confirms the identified result without prior knowledge or additional data. Identification of the single unknown in the original dynamic equations is then reduced to a straightforward exercise with two-stage VSI, which

we have described for algebraic and differential operators, respectively. Combining the dynamic data with the high spatial resolution steady state data is also advantageous in identifying extreme cases such as very small parameters. We direct the reader to Section B and Tables 8-11 in the Appendix where the relevant results have been presented. Thus, in cases wherein steady state (or near-steady state) data are available, they serve as a “zeroth” step to be followed by only one of the stages that have been laid out for dynamic data in Section 2. If the dynamics remain far from steady state, the two-stage VSI is still applicable, given snapshots at sufficiently many time instants.

The challenge for system identification lies in selecting the correct operators from a large library of candidates. In our experience, the failure to identify the correct operators usually precedes the poor inference of coefficients, since the algorithms are then left with representing the data with the wrong model. In this communication we demonstrated our methods using synthetic data, and compared the identified models with the true models. In practice, quantifying the uncertainty becomes extremely important when using real world data. In this work we also assumed that the physics is governed by first-order dynamics. The Confirmation Test may provide an avenue to system identification without this assumption, enabling the discernment of first-order in time, parabolic, PDEs from second-order, hyperbolic PDEs.

We also note that system identification is significantly more challenging if greater numbers of candidate bases are retained. In this case, stepwise regression is robust as it iteratively eliminates inactive operators instead of attempting to find a solution in “one shot”, thus mollifying the problem to a degree. Given the larger number of operator bases, the loss would be small and remain flat for several iterations before the model become underfit. However, VSI also suffers from missing key operators, similar to related methods such as SINDy [26]. In this case, VSI would find the “closest” governing system where the missing basis are compensated by a larger number of other basis terms that are being considered. However difficulties may arise from non-unique combinations, and non-sparse solutions. We also anticipate that the loss will show many jumps indicating that operators that do contribute to the model have been eliminated in these iterations.

Finally, we note that apart from assuming first-order dynamics, we have not imposed conditions to constrain the identified system of equations to be parabolic. This brings up an important question of stability. We have shown numerical comparisons in Figure 16 where the identified system predicts a solution field that is similar, but not identical to the original data. Large errors in system identification can lead to instabilities in the solution. Such instabilities can be controlled by imposing constraints on combinations of coefficients in the library of operators. In other approaches (to appear soon) we have developed methods of staggering and “round robin” operator suppression to eliminate system instabilities. A third approach worth exploration would be to incorporate forward trajectories computed from the inferred system in the loss function.

Acknowledgements

We acknowledge the support of Toyota Research Institute, Award #849910, “Computational framework for data-driven, predictive, multi-scale and multi-physics modeling of battery materials” (ZW and KG). Additional support: This material is based upon work supported by the Defense Advanced Research Projects Agency (DARPA) under Agreement No. HR0011199002, “Artificial Intelligence guided multi-scale multi-physics framework for discovering complex emergent materials phenomena” (ZW, XH and KG).

References

1. T. Jiang, S. Rudraraju, A. Roy, A. Van der Ven, K. Garikipati, and M. L. Falk. Multi-physics simulations of lithiation-induced stress in litio electrode particles. *J. Phys. Chem. C*, 120, 2016.
2. S. Rudraraju, A. Van der Ven, and K. Garikipati. Mechano-chemical spinodal decomposition: A phenomenological theory of phase transformations in multi-component crystalline solids. *Nature Computational Materials*, 2, 2016.
3. G.H. Teichert, S. Rudraraju, and K. Garikipati. A variational treatment of material configurations with application to interface motion and microstructural evolution. *Journal of the Mechanics and Physics of Solids*, 99, 2017.
4. J. W. Cahn and J. E. Hilliard. Free energy of a nonuniform system. i interfacial energy. *J. Chem. Phys.*, 28, 1958.
5. A. M. Turing. The chemical basis of morphogenesis. *Phil. Trans. Roy. Soc. Lond. Ser. B.*, 237, 1952.
6. A. Gierer and H. Meinhardt. A theory of biological pattern formation. *Kybernetik*, 12, 1972.
7. J. D. Murray. On pattern formation mechanisms for lepidopteran wing patterns and mammalian coat markings. *Phil. Trans. Roy. Soc. Lond. Ser. B*, 295, 1981.
8. R. Dillon, P. K. Maini, and H. G. Othmer. Pattern formation in generalized turing systems i: Steady-state patterns in systems with mixed boundary conditions. *J. Math. Biol.*, 32, 1994.
9. R. A. Barrio, C. Varea, and J. L. Aragon. A two-dimensional numerical study of spatial pattern formation in interacting turing systems. *Bull. Math. Biol.*, 61, 1999.
10. R. A. Barrio, R. E. Baker, B. Vaughan, K. Tribuzy, M. R. de Carvalho, Rodney Bassanezi, and P. K. Maini. Modeling the skin pattern of fishes. *Phys. Rev. E*, 79, 2009.

11. Philip K. Maini, Thomas E. Woolley, Ruth E. Baker, Eamonn A. Gaffney, and S. Seirin Lee. Turing’s model for biological pattern formation and the robustness problem. *Interface Focus*, 2(4):487–496, 2012. doi: 10.1098/rsfs.2011.0113.
12. F. Spill, P. Guerrero, T. Alarcon, P. K. Maini, and H. Byrne. Hybrid approaches for multiple-species stochastic reaction-diffusion models. *J. Comput. Phys.*, 299, 2015.
13. K. Korvasová, E. A. Gaffney, P. K. Maini, M. A. Ferreira, and V. Klika. Investigating the turing conditions for diffusion-driven instability in the presence of a binding immobile substrate. *J. Theor. Biol.*, 367, 2015.
14. K. Garikipati. Perspectives on the mathematics of biological patterning and morphogenesis. *J. Mech. Phys. Solids.*, 99, 2017.
15. S. M. Wise, J. S. Lowengrub, H. B. Frieboes, and V. Cristini. Three-dimensional multispecies nonlinear tumor growth—model and numerical method. *J. Theor. Biol.*, 253, 2008.
16. V. Cristini, X. Li, J. S. Lowengrub, and S. M. Wise. Nonlinear simulations of solid tumor growth using a mixture model: invasion and branching. *J. Math. Biol.*, 58, 2009.
17. J. S. Lowengrub, H. B. Frieboes, F. Jin, Y-L. Chuang, X. Li, Macklin, S. M. Wise, and V. Cristini. Nonlinear modelling of cancer: bridging the gap between cells and tumours. *Nonlinearity*, 23, 2010.
18. J. S. Lowengrub, A. Rätz, and A. Voigt. Phase-field modeling of the dynamics of multicomponent vesicles: Spinodal decomposition, coarsening, budding, and fission. *Phys. Rev. E*, 79, 2009.
19. G. Vilanova, I. Colominas, and H. Gomez. Capillary networks in tumor angiogenesis: From discrete endothelial cells to phase-field averaged descriptions via isogeometric analysis. *Num. Meth. Biomed. Eng.*, 29, 2013.
20. G. Vilanova, I. Colominas, and H. Gomez. Coupling of discrete random walks and continuous modeling for three-dimensional tumor-induced angiogenesis. *Comput. Mech.*, 53, 2014.
21. J. T. Oden, A. Hawkins, and S. Prudhomme. General diffuse-interface theories and an approach to predictive tumor growth modeling. *Math. Mod. Meth. App. Sci.*, 20, 2010.
22. J. Xu, G. Vilanova, and H. Gomez. A mathematical model coupling tumor growth and angiogenesis. *PLoS ONE*, 11, 2016.
23. R. HilleRisLambers, M. Rietkerk, F. van den Bosch, H.H.T. Prins, and H. de Kroon. Vegetation pattern formation in semi-arid grazing systems. *Ecol.*, 82:50–61, 2001.

24. M. Rietkerk and J. van de Koppel. Regular pattern formation in real ecosystems. *Trends Ecol. Evol.*, 23:169–175, 2008.
25. Steve Brooks, Andrew Gelman, Galin Jones, and Xiao-Li Meng, editors. *Handbook of Markov Chain Monte Carlo*. Chapman and Hall/CRC, 2011. ISBN 978-1-4200-7941-8. doi: 10.1201/b10905.
26. S. L. Brunton, J. L. Proctor, and J. N. Kutz. Discovering governing equations from data by sparse identification of nonlinear dynamical systems. *Proc. Natl. Acad. Sci.*, 113, 2016.
27. Z. Wang, X. Huan, and K. Garikipati. Variational system identification of the partial differential equations governing the physics of pattern-formation: Inference under varying fidelity and noise. *Computer Methods in Applied Mechanics and Engineering*, 356:44 – 74, 2019. ISSN 0045-7825. doi: <https://doi.org/10.1016/j.cma.2019.07.007>.
28. N. M. Mangan, S. L. Brunton, J. L. Proctor, and J. N. Kutz. Inferring biological networks by sparse identification of nonlinear dynamics. *IEEE Trans. Mol. Biol. Multi-Scale Commun.*, 2, 2016.
29. S. H. Rudy, S. L. Brunton, J. L. Proctor, and J. N. Kutz. Data-driven discovery of partial differential equations. *Sci. Adv.*, 3, 2017.
30. M. Raissi, P. Perdikaris, and G.E. Karniadakis. Physics-informed neural networks: A deep learning framework for solving forward and inverse problems involving nonlinear partial differential equations. *J. Comput. Phys.*, 378, 2019.
31. Z. Wang, B. Wu X. Huan, and K. Garikipati. A perspective on regression and bayesian approaches for system identification of pattern formation dynamics. *Theoretical Appl. Mech. Lett.*, 2020. To appear.
32. Steven Atkinson, Liping Wang Waad Subber, Genghis Khan, Philippe Hawi, and Roger Ghanem. Data-driven discovery of free-form governing differential equations. *Second Workshop on Machine Learning and the Physical Sciences*, 2019.
33. Or Yair, Ronen Talmon, Ronald R. Coifman, and Ioannis G. Kevrekidis. Reconstruction of normal forms by learning informed observation geometries from data. *Proceedings of the National Academy of Sciences*, 114(38):E7865–E7874, 2017. doi: 10.1073/pnas.1620045114.
34. Patrick A. K. Reinbold, Daniel R. Gurevich, and Roman O. Grigoriev. Using noisy or incomplete data to discover models of spatiotemporal dynamics. *Phys. Rev. E*, 101:010203, Jan 2020. doi: 10.1103/PhysRevE.101.010203.

35. Daniel A. Messenger and David M. Bortz. Weak sindy: Galerkin-based data-driven model selection. *arXiv:2005.04339*, 2020.
36. Daniel A. Messenger and David M. Bortz. Weak sindy for partial differential equations. *arXiv:2007.02848*, 2020.
37. J. Cottrell, T. Hughes, and Y. Bazilevs. Isogeometric analysis: Toward integration of cad and fea. *Wiley, Chichester*, 2009.
38. Emmanuel J. Candès, Justin Romberg, and Terence Tao. Robust Uncertainty Principles: Exact Signal Reconstruction From Highly Incomplete Frequency Information. *IEEE Transactions on Information Theory*, 52(2):489–509, 2006. ISSN 0018-9448. doi: 10.1109/TIT.2005.862083.
39. David L. Donoho. Compressed sensing. *IEEE Transactions on Information Theory*, 52(4):1289–1306, 2006. ISSN 00189448. doi: 10.1109/Tit.2006.871582.
40. G. James, D. Witten, T. Hastie, and R. Tibshirani. An introduction to statistical learning. *Springer New York, Inc., New York, NY, USA.*, 2013.
41. N. M. Mangan, J. N. Kutz, S. L. Brunton, and J. L. Proctor. Model selection for dynamical systems via sparse regression and information criteria. *Proceedings of the Royal Society A: Mathematical, Physical and Engineering Sciences*, 473(2204):20170009, 2017. doi: 10.1098/rspa.2017.0009.
42. J. Schnakenberg. Network theory of microscopic and macroscopic behavior of master equation systems. *Rev. Mod. Phys.*, 48, 1976.
43. M. Schmidt and H. Lipson. Distilling free-form natural laws from experimental data. *Science*, 03, 2009.
44. M. D Schmidt, R. R Vallabhajosyula, J. W Jenkins, J. E Hood, A. S Soni, J P Wikswo, and H. Lipson. Automated refinement and inference of analytical models for metabolic networks. *Phys. Biol.*, 8, 2011.
45. Samuel M. Allen and John W. Cahn. A microscopic theory for antiphase boundary motion and its application to antiphase domain coarsening. *Acta Metall.*, 27, 1979.

Appendix

A Similarity of snapshots in Cahn-Hilliard and Allen-Cahn Equations

In this section, we numerically validate our assumptions of similarity between snapshots for the other two types of PDEs that commonly used to model pattern formation. For the ease of the reader, we restate the two assumptions we made:

$$\left| \int_{\bar{\Omega}^I} \mathbf{j} \cdot \mathbf{n} dS \right| \leq \varepsilon_b, \quad i = 1, 2 \quad (80)$$

and

$$\left| \frac{1}{\bar{V}^I} \int_{\bar{\Omega}^I} C^k dV - \frac{1}{\bar{V}^J} \int_{\bar{\Omega}^J} C^k dV \right| \leq \varepsilon_r. \quad (81)$$

Relation (80) indicates that the total flux vanishes and Relation (81) indicates that the powers of the concentration field within one snapshot can be approximated by the data over another spatially unrelated snapshot.

We restate the Cahn-Hilliard equations (Model 2 in the main document):

$$\frac{\partial C_1}{\partial t} = \nabla \cdot (M_1 \nabla \mu_1) \quad (82)$$

$$\frac{\partial C_2}{\partial t} = \nabla \cdot (M_2 \nabla \mu_2) \quad (83)$$

$$\mu_1 = \frac{\partial g}{\partial C_1} - k_1 \nabla^2 C_1 \quad (84)$$

$$\mu_2 = \frac{\partial g}{\partial C_2} - k_2 \nabla^2 C_2 \quad (85)$$

$$\text{with } \nabla \mu_1 \cdot \mathbf{n} = 0; \nabla C_1 \cdot \mathbf{n} = 0 \text{ on } \Gamma \quad (86)$$

$$\nabla \mu_2 \cdot \mathbf{n} = 0; \nabla C_2 \cdot \mathbf{n} = 0 \text{ on } \Gamma \quad (87)$$

and g is the non-convex, “homogeneous” free energy density function, whose form has been chosen as

$$\begin{aligned} g(C_1, C_2) = & \frac{3d}{2s^4} ((2C_1 - 1)^2 + (2C_2 - 1)^2)^2 + \frac{d}{s^3} (2C_2 - 1) ((2C_2 - 1)^2 - 3(2C_1 - 1)^2) \\ & - \frac{3d}{2s^2} ((2C_1 - 1)^2 + (2C_2 - 1)^2). \end{aligned} \quad (88)$$

The Allen-Cahn equation [45] is another type of parabolic PDE that is commonly used to model pattern formation. This following is a coupled Cahn-Hilliard/Allen-Cahn equations system where the field C_2 describes growth of alloy precipitates from nuclei created by a process of spinodal decomposition and Ostwald ripening that control the field C_1 .

$$\frac{\partial C_1}{\partial t} = \nabla \cdot (M_1 \nabla \mu_1) \quad (89)$$

$$\frac{\partial C_2}{\partial t} = -M_2 \mu_2 \quad (90)$$

$$\mu_1 = \frac{\partial g}{\partial C_1} - \nabla \cdot k_1 \nabla C_1 \quad (91)$$

$$\mu_2 = \frac{\partial g}{\partial C_2} - \nabla \cdot k_2 \nabla C_2 \quad (92)$$

$$\text{with } \nabla \mu_1 \cdot \mathbf{n} = 0; \nabla C_1 \cdot \mathbf{n} = 0 \text{ on } \Gamma \quad (93)$$

$$\nabla C_2 \cdot \mathbf{n} = 0 \text{ on } \Gamma \quad (94)$$

The free energy density $g(C_1, C_2)$ couples these processes through μ_1 and μ_2 . An important difference from Cahn-Hilliard equations is that C_2 is a non-conserved order parameter, which defines the identities of the precipitate, described by composition field C_1 , and matrix phases. The parameters are summarized in Table 7.

M_1	M_2	k_1	k_2	d	s
0.1	0.1	10	10	0.4	0.7

Table 7: parameters used in the simulations.

Figure 17 shows the patterns formed by Cahn-Hilliard and Allen-Cahn equations, with “particles” and short stripes randomly distributed over the domain. We first evaluate the total flux of snapshots of different sizes shown in Figure 18. As the snapshot size increases, the flux scaled by its volume vanishes for both Cahn-Hilliard and Allen-Cahn equations. This validates the relation (81). Figures 19 and 20 show the first and second powers of C_1 and C_2 , evaluated using data with different sizes of snapshots from separate simulations of Cahn-Hilliard and Allen-Cahn equations. Random perturbations in the initial conditions affect the local features of C_1 and C_2 ; however, with increasing size of snapshots their similarity becomes evident. Consequently powers evaluated using data from snapshots converge to the values obtained by using full field data on the entire domain. This validates Relation (81).

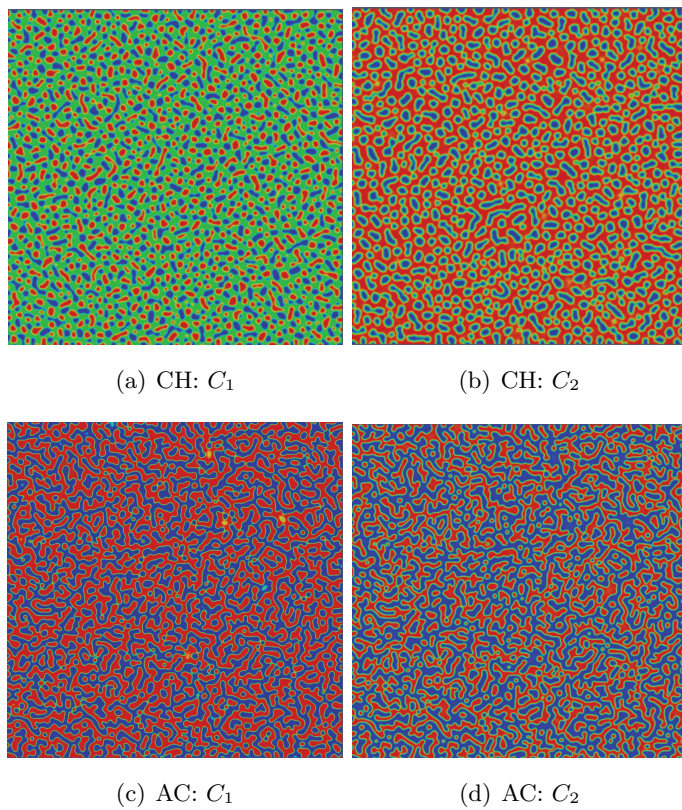
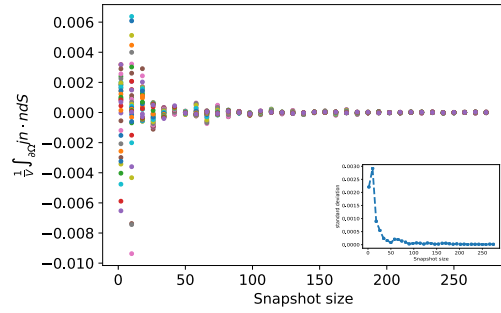
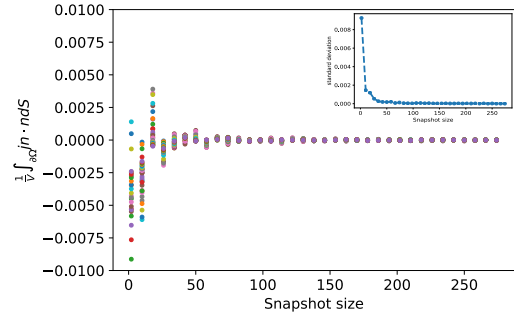


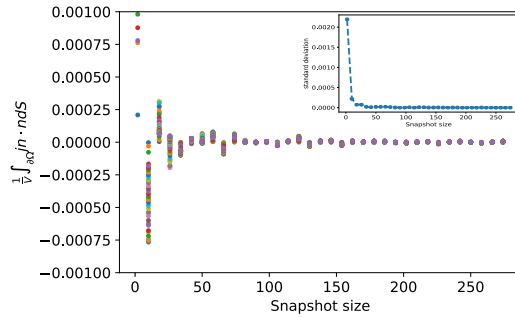
Figure 17: The upper plots show the patterning of “particles” by Cahn-Hilliard equation, and the lower plots shows the patterning of short stripes by Allen-Cahn equations.



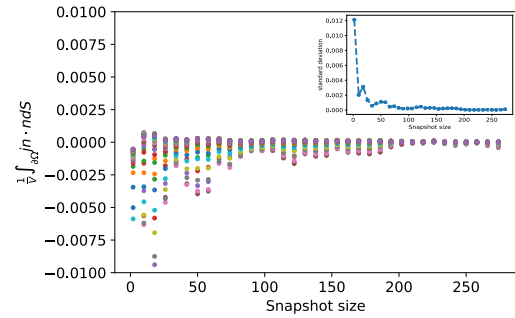
(a) CH: total flux for C_1 concentration



(b) CH: total flux for C_2 concentration

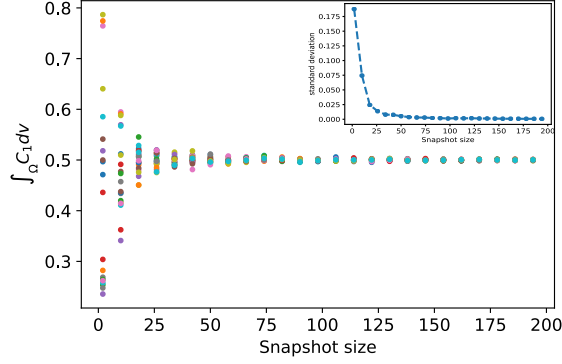


(c) AC: total flux for C_1 concentration

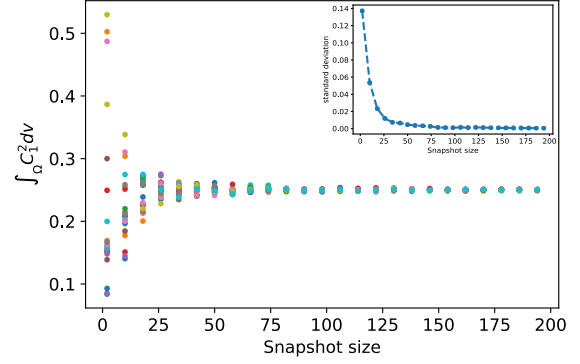


(d) AC: total flux for C_2 concentration

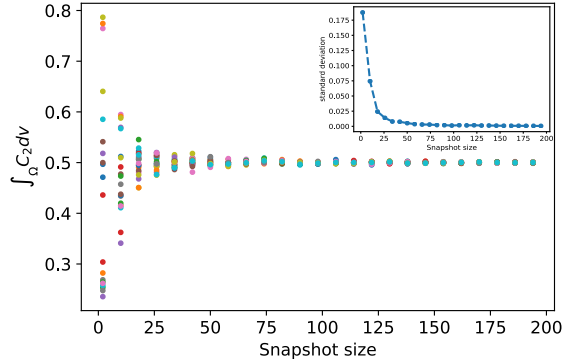
Figure 18: The total flux across the boundaries with different snapshot sizes with the Cahn-Hilliard (upper plots) and Allen-Cahn equations (lower plots) marked by different colors. The total flux converges to zero with increasing snapshot size. The embedded subplot shows the decreasing standard deviation.



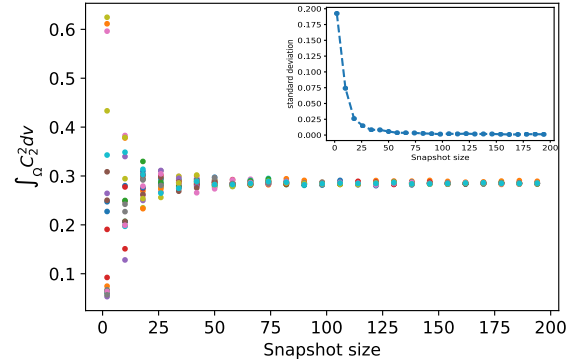
(a) First power of C_1



(b) Second power C_1^2

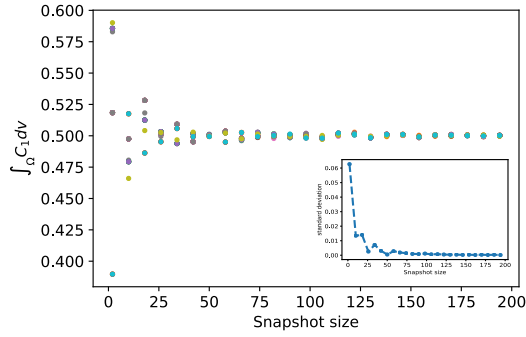


(c) First power of C_2

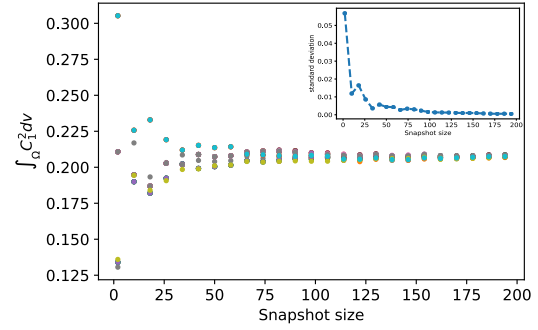


(d) Second power C_2^2

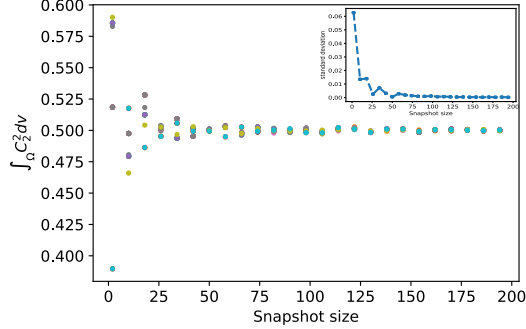
Figure 19: The powers evaluated using data generated by Cahn-Hilliard equations from 30 simulations, marked by different colors, with different randomized initial conditions modeling data from different specimens. The embedded subplot shows the decreasing standard deviation of moments. In the main and sub-plot, note the convergence with increasing snapshot size.



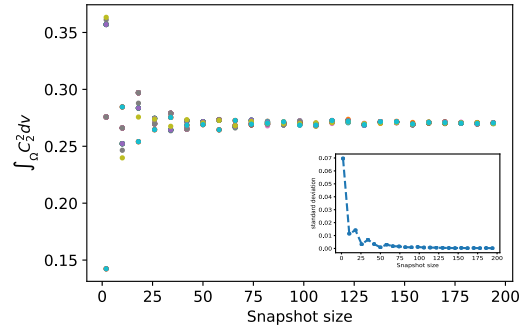
(a) First power of C_1



(b) Second power C_1^2



(c) First power of C_2



(d) Second power C_2^2

Figure 20: The powers evaluated using data generated by Allen-Cahn equations from 30 simulations, marked by different colors, with different randomized initial conditions modeling data from different specimens. The embedded subplot shows the decreasing standard deviation of moments. In the main and sub-plot, note the convergence with increasing snapshot size.

B System identification of models with small parameters

In this section we studied the diffusion-reaction system (Model 1 in the main document) with the same reaction term, but smaller coefficients for diffusion terms. We restate the model here:

$$\frac{\partial C_1}{\partial t} = D_1 \nabla^2 C_1 + R_{10} + R_{11} C_1 + R_{13} C_1^2 C_2 \quad (95)$$

$$\frac{\partial C_2}{\partial t} = D_2 \nabla^2 C_2 + R_{20} + R_{21} C_1^2 C_2 \quad (96)$$

$$\text{with } \nabla C_1 \cdot \mathbf{n} = 0; \quad \nabla C_2 \cdot \mathbf{n} = 0 \text{ on } \Gamma \quad (97)$$

where Γ is the domain boundary.

We generate two data sets using models i) with $D_1 = 0.1$ and $D_2 = 4$ and ii) with $D_1 = 0.001$ and $D_2 = 0.04$. The coefficients used for reaction terms are summarized in Table 8. The data are again collected at 30 time steps, each over a spatially unrelated snapshot from a different simulation. We also collect one steady state data set for the case with $D_1 = 0.001$ and $D_2 = 0.04$.

R_{10}	R_{11}	R_{13}	R_{20}	R_{21}
0.1	-1	1	0.9	-1

Table 8: True parameter values used in DNS for synthesizing test data.

Using the dynamic data, we successfully identify all the reaction terms for both cases in Stage 1 (See Tables 9 and 10). This is because the two stage VSI eliminates the effects of gradient-dependent operators at the first stage. For the case with relatively higher diffusivities, we are able to identify the diffusion term using the 100×100 and larger snapshots. However with the 50×50 dataset, the Laplacian operator is incorrectly eliminated and another operator is selected eventually. For the case with $D_1 = 0.001$, $D_2 = 0.04$, VSI failed to identify the Laplacian operator using all datasets. However, given access to steady state data, the Laplacian operator can be uncovered correctly using the Confirmation Test for the case with $D_1 = 0.001$, $D_2 = 0.04$ (See Table 11). This is because the high spatial resolution of the data at steady state can much more accurately resolve gradient operators.

It is challenging to identify operators that have much smaller contributions (e.g. the operators with extremely small coefficients). This is particularly true with noise that may wash out the true values of the operators constructed from the data. Splitting the process into two stages by the judicious choices of weighting functions can eliminate the effects of certain operators at different stages. Recently, it has been shown that variational system identification can successfully identify the model using data with large levels of noise (greater than 10%) by exploiting the form of the weighting function [35, 36].

mesh size	results
400 × 400	$\int_{\Omega} w_1 \frac{\partial C_1}{\partial t} dv = \int_{\Omega} -0.1004 \nabla w_1 \cdot \nabla C_1 dv + \int_{\Omega} w_1 (0.10006 - 0.99995 C_1 + 0.99994 C_1^2 C_2) dv$ $\int_{\Omega} w_2 \frac{\partial C_2}{\partial t} dv = \int_{\Omega} -3.85 \nabla w_2 \cdot \nabla C_2 dv + \int_{\Omega} w_2 (0.9005 - 1.0004 C_1^2 C_2) dv$
300 × 300	$\int_{\Omega} w_1 \frac{\partial C_1}{\partial t} dv = \int_{\Omega} -0.1005 \nabla w_1 \cdot \nabla C_1 dv + \int_{\Omega} w_1 (0.09998 - 0.9999 C_1 + 0.9999 C_1^2 C_2) dv$ $\int_{\Omega} w_2 \frac{\partial C_2}{\partial t} dv = \int_{\Omega} -3.85 \nabla w_2 \cdot \nabla C_2 dv + \int_{\Omega} w_2 (0.9007 - 0.9998 C_1^2 C_2) dv$
200 × 200	$\int_{\Omega} w_1 \frac{\partial C_1}{\partial t} dv = \int_{\Omega} -0.05 \nabla w_1 \cdot \nabla C_1 dv + \int_{\Omega} w_1 (0.10005 - 1.0003 C_1 + 1.0001 C_1^2 C_2) dv$ $\int_{\Omega} w_2 \frac{\partial C_2}{\partial t} dv = \int_{\Omega} -3.86 \nabla w_2 \cdot \nabla C_2 dv + \int_{\Omega} w_2 (0.9005 - 0.9999 C_1^2 C_2) dv$
100 × 100	$\int_{\Omega} w_1 \frac{\partial C_1}{\partial t} dv = \int_{\Omega} -0.1003 \nabla w_1 \cdot \nabla C_1 dv + \int_{\Omega} w_1 (0.09975 - 0.9997 C_1 + 0.9997 C_1^2 C_2) dv$ $\int_{\Omega} w_2 \frac{\partial C_2}{\partial t} dv = \int_{\Omega} -1.34 \nabla w_2 \cdot \nabla C_2 dv + \int_{\Omega} w_2 (0.9001 - 1.0001 C_1^2 C_2) dv$
50 × 50	$\int_{\Omega} w_1 \frac{\partial C_1}{\partial t} dv = \int_{\Omega} 0.0076 \nabla w_1 \cdot \nabla C_1 dv + \int_{\Omega} w_1 (0.0999 - 0.9991 C_1 + 0.9993 C_1^2 C_2) dv$ $\int_{\Omega} w_2 \frac{\partial C_2}{\partial t} dv = \int_{\Omega} -1.48 \nabla w_2 \cdot \nabla C_2 dv + \int_{\Omega} w_2 (0.8997 - 0.99994 C_1^2 C_2) dv$

Table 9: Results using noise-free dynamic data generated from Model 1 with $D_1 = 0.1, D_2 = 4$.

mesh size	results
400 × 400	$\int_{\Omega} w_1 \frac{\partial C_1}{\partial t} dv = \int_{\Omega} -0.00161 \nabla w_1 \cdot \nabla C_1 dv + \int_{\Omega} w_1 (0.100038 - 1.00003 C_1 + 1.000035 C_1^2 C_2) dv$ $\int_{\Omega} w_2 \frac{\partial C_2}{\partial t} dv = \int_{\Omega} -0.043 \nabla w_2 \cdot \nabla C_2 dv + \int_{\Omega} w_2 (-0.8999 - 1.00005 C_1^2 C_2) dv$
300 × 300	$\int_{\Omega} w_1 \frac{\partial C_1}{\partial t} dv = \int_{\Omega} -0.00162 \nabla w_1 \cdot \nabla C_1 dv + \int_{\Omega} w_1 (0.09995 - 0.99993 C_1 + 1.00004 C_1^2 C_2) dv$ $\int_{\Omega} w_2 \frac{\partial C_2}{\partial t} dv = \int_{\Omega} -0.044 \nabla w_2 \cdot \nabla C_2 dv + \int_{\Omega} w_2 (-0.9001 - 1.0002 C_1^2 C_2) dv$
200 × 200	$\int_{\Omega} w_1 \frac{\partial C_1}{\partial t} dv = \int_{\Omega} -0.00164 \nabla w_1 \cdot \nabla C_1 dv + \int_{\Omega} w_1 (0.0997 - 0.9995 C_1 + 0.9996 C_1^2 C_2) dv$ $\int_{\Omega} w_2 \frac{\partial C_2}{\partial t} dv = \int_{\Omega} -0.044 \nabla w_2 \cdot \nabla C_2 dv + \int_{\Omega} w_2 (-0.9001 - 1.0002 C_1^2 C_2) dv$
100 × 100	$\int_{\Omega} w_1 \frac{\partial C_1}{\partial t} dv = \int_{\Omega} -0.00064 \nabla w_1 \cdot \nabla C_1 dv + \int_{\Omega} w_1 (0.09975 - 1.0012 C_1 + 1.0014 C_1^2 C_2) dv$ $\int_{\Omega} w_2 \frac{\partial C_2}{\partial t} dv = \int_{\Omega} -0.044 \nabla w_2 \cdot \nabla C_2 dv + \int_{\Omega} w_2 (-0.901 - 1.0003 C_1^2 C_2) dv$
50 × 50	$\int_{\Omega} w_1 \frac{\partial C_1}{\partial t} dv = \int_{\Omega} -0.0017 \nabla w_1 \cdot \nabla C_1 dv + \int_{\Omega} w_1 (-0.0999 - 0.9991 C_1 + 0.9993 C_1^2 C_2) dv$ $\int_{\Omega} w_2 \frac{\partial C_2}{\partial t} dv = \int_{\Omega} -0.024 \nabla w_2 \cdot \nabla C_2 dv + \int_{\Omega} w_2 (-0.898 - 0.9991 C_1^2 C_2) dv$

Table 10: Results using noise-free dynamic data generated from Model 1 with $D_1 = 0.001, D_2 = 0.04$.

mesh size	results
400 × 400	$\int_{\Omega} w_1 \frac{\partial C_1}{\partial t} dv = \int_{\Omega} -0.00100005 \nabla w_1 \cdot \nabla C_1 dv + \int_{\Omega} w_1 (0.100038 - 1.00003 C_1 + 1.000035 C_1^2 C_2) dv$ $\int_{\Omega} w_2 \frac{\partial C_2}{\partial t} dv = \int_{\Omega} -0.040002 \nabla w_2 \cdot \nabla C_2 dv + \int_{\Omega} w_2 (-0.8999 - 1.00005 C_1^2 C_2) dv$
300 × 300	$\int_{\Omega} w_1 \frac{\partial C_1}{\partial t} dv = \int_{\Omega} -0.0010003 \nabla w_1 \cdot \nabla C_1 dv + \int_{\Omega} w_1 (0.09995 - 0.99993 C_1 + 1.00004 C_1^2 C_2) dv$ $\int_{\Omega} w_2 \frac{\partial C_2}{\partial t} dv = \int_{\Omega} -0.04000867 \nabla w_2 \cdot \nabla C_2 dv + \int_{\Omega} w_2 (-0.9001 - 1.0002 C_1^2 C_2) dv$
200 × 200	$\int_{\Omega} w_1 \frac{\partial C_1}{\partial t} dv = \int_{\Omega} -0.00099984 \nabla w_1 \cdot \nabla C_1 dv + \int_{\Omega} w_1 (0.0997 - 0.9995 C_1 + 0.9996 C_1^2 C_2) dv$ $\int_{\Omega} w_2 \frac{\partial C_2}{\partial t} dv = \int_{\Omega} -0.04000868 \nabla w_2 \cdot \nabla C_2 dv + \int_{\Omega} w_2 (-0.9001 - 1.0002 C_1^2 C_2) dv$
100 × 100	$\int_{\Omega} w_1 \frac{\partial C_1}{\partial t} dv = \int_{\Omega} -0.00100208 \nabla w_1 \cdot \nabla C_1 dv + \int_{\Omega} w_1 (0.09975 - 1.0012 C_1 + 1.0014 C_1^2 C_2) dv$ $\int_{\Omega} w_2 \frac{\partial C_2}{\partial t} dv = \int_{\Omega} -0.04001184 \nabla w_2 \cdot \nabla C_2 dv + \int_{\Omega} w_2 (-0.901 - 1.0003 C_1^2 C_2) dv$
50 × 50	$\int_{\Omega} w_1 \frac{\partial C_1}{\partial t} dv = \int_{\Omega} -0.00099981 \nabla w_1 \cdot \nabla C_1 dv + \int_{\Omega} w_1 (-0.0999 - 0.9991 C_1 + 0.9993 C_1^2 C_2) dv$ $\int_{\Omega} w_2 \frac{\partial C_2}{\partial t} dv = \int_{\Omega} -0.0399638 \nabla w_2 \cdot \nabla C_2 dv + \int_{\Omega} w_2 (-0.898 - 0.9991 C_1^2 C_2) dv$

Table 11: Results using noise-free steady state and dynamic data generated from Model 1 with $D_1 = 0.001, D_2 = 0.04$.